

Using Machine Learning for Scientific Discovery in Electronic Quantum Matter Visualization Experiments

Yi Zhang^{1,*}, A. Mesaros^{1,2,*}, K. Fujita³, S.D. Edkins^{1,4}, M.H. Hamidian^{1,5}, K. Ch'ng⁶, H. Eisaki⁷, S. Uchida^{7,8}, J.C. Séamus Davis^{1,3,9,10}, E. Khatami⁶ and Eun-Ah Kim¹

¹ LASSP, Department of Physics, Cornell University, Ithaca, NY 14853, USA.

² Laboratoire de Physique des Solides, CNRS, Université Paris-Sud, 91405 Orsay Cedex, France.

³ CMPMS Department, Brookhaven National Laboratory, Upton, NY 11973, USA.

⁴ Department of Applied Physics, Stanford University, Stanford, CA 94305, USA.

⁵ Department of Physics, Harvard University, Cambridge, MA 02138, USA.

⁶ Department of Physics and Astronomy, San Jose State University, San Jose, CA 95192, USA.

⁷ Institute of Advanced Industrial Science and Technology, Tsukuba, Ibaraki 305-8568, Japan.

⁸ Department of Physics, University of Tokyo, Bunkyo-ku, Tokyo 113-0033, Japan.

⁹ Department of Physics, University College Cork, Cork T12R5C, Ireland

¹⁰ Department of Physics, Oxford University, Oxford, OX1 3PU, UK

* These authors contributed equally to this work.

Essentials of the scientific discovery process have remained largely unchanged for centuries¹: systematic human observation of natural phenomena is used to form hypotheses that, when validated through experimentation, are generalized into established scientific theory. Today, however, we face major scientific challenges because automated scientific instrumentation and large-scale data acquisition are generating data sets of such volume and complexity as to defy human analysis. To achieve scientific discovery using these enormous empirical data sets will require new approaches^{2,3}. A good example is modern visualization studies of electronic quantum matter (EQM) which yield dense arrays of electronic structure images that are often astonishingly complex at the atomic-scale⁴. Given the recent advances in machine learning (ML) for the study of synthetically generated classical and quantum states of matter⁵⁻¹⁶, the outstanding challenge now is to engage ML with real EQM data. Here we report development and training of an array of artificial neural networks (ANN) designed to recognize different types of hypothesized order hidden in EQM image-arrays. The ANNs are used to analyze a large, experimentally-

derived EQM image archive, spanning a wide range of electron densities and energies, in carrier-doped cuprate Mott insulators. Remarkably, this ANN array repeatedly and reliably reveals throughout the noisy and complex data, the existence of a lattice-commensurate, precisely four-unit-cell periodic, translational-symmetry-breaking EQM state. Further, the ANNs discover that the highly disordered modulations of this state are nevertheless strongly unidirectional, meaning that a nematic or rotational-symmetry-breaking EQM state coincides with it. These phenomena are all consistent with strong-coupling theories of electronic liquid crystals^{17,18} in such materials. This marks a significant advance in the capability of ML to achieve physics discovery and reveals exciting new avenues for efficient hypothesis testing in large scale EQM research.

1 Automation of scientific apparatus and high capacity data-acquisition have revolutionized the empirical approach to many sciences including for example astronomy, elementary particles, genomics, climatology, materials science and quantum matter research. In many cases, the resulting “big” data sets have already become far too large for any team of human beings to examine in detail, are often created without objective conceptual procedures for how to extract the fundamental knowledge therein, and yet they contain unsurpassed empirical information on many scientifically, societally and economically important subjects. Novel scientific approaches are urgently required to deal with the issues of volume, complexity and objectivity in analysis of these enormous experimental data sets. Globally, this has motivated urgent research initiatives within and across disciplines, whose strategic objectives are to develop machine learning techniques for use directly in the scientific discovery process¹⁹. Rapid progress is occurring in materials science, where, for example, ML is used to analyze synthetic chemical and structural data, seeking predictability in empirical properties such as metallicity²⁰, superconductivity²¹ and dynamics of crystalline defects²²; and for high-throughput

exploration of molecules²³ and materials such as magnetics²⁴. However, although of urgent interest and great promise, ML discoveries based on experimental data in EQM research have so far been lacking.

2 Crystalline solids contain many different types of EQM and familiar among them are simple metals, semiconductors, ferromagnets, superconductors and density waves. These have been well understood for decades²⁵ using theoretical approaches that describe each electron as a quantum mechanical wave state with a definite momentum. Today's research frontier is concentrated, instead, on the exotic forms of EQM that emerge when electrons interact so strongly that they can no longer be associated with a definite momentum. These electrons often self-organize into complex and unanticipated new states of EQM including, for example, electronic liquid crystal^{17,18}, high temperature superconductors^{26,27}, fractionalized electronic fluids²⁸ and quantum spin liquids²⁹. In these forms of EQM, astronomical numbers of strongly interacting electrons exhibit unprecedented "social" behaviors which are often difficult to predict and challenging to understand. Vast experimental data sets have begun to appear in this field, for example from real space (\mathbf{r} -space) visualization of EQM using spectroscopic imaging scanning tunneling microscopy⁴ (SISTM), from momentum space (\mathbf{k} -space) visualization of EQM using angle resolved photoemission (ARPES), or from modern X-ray and neutron scattering facilities. Consequently, we face an urgent and growing challenge to develop ML strategies capable of scientific discovery using the enormous and complex experimental data structures derived from modern condensed matter physics research.

3 For example, the electronic structure of the CuO₂ plane in the cuprate compounds supporting very high temperature superconductivity²⁶ (Fig. 1A) is one of the deepest problems in EQM studies today. With one electron per Cu site, strong Coulomb interactions between electrons produce charge localization in an antiferromagnetic Mott insulator (MI)

state. Removing p electrons (adding p ‘holes’) per CuO₂ plaquette generates the ‘pseudogap’ phase^{30,31}, a state with strongly depleted density-of-electronic states $N(E)$ for energies $-\Delta_1 < E < \Delta_1$ where Δ_1 is the characteristic pseudogap energy scale. This PG state exists at temperatures below the characteristic pseudogap temperature $T^*(p)$ (Fig. 1A) at which the pseudogap opens in the spectrum of electronic excitations^{30,31}. Eventually, at higher p , the d -symmetry high temperature superconductivity (SC) appears (Fig. 1A) and understanding the enhancement of its maximum critical temperature T_c is the long-term strategic goal for the whole field. However, the PG phase which appears to constrain the highest T_c has defied microscopic identification for three decades. Recently, it has been widely reported that rotational and translational symmetry are spontaneously broken in this phase. The rotational symmetry breaking is referred to as a nematic (NE) state^{4,17,32,33}; it occurs at wavevector $\mathbf{Q}=0$ as the breaking of 90°-rotational (C_4) symmetry and appears at $T^*(p)$ (Fig. 1A) where the pseudogap opens^{4,26,30,31}. This is a long-standing conundrum because, in theory, ordering at $\mathbf{Q}=0$ cannot open an energy gap in the electronic spectrum. The translational symmetry breaking or density wave (DW) state, which can open such an energy gap, is now detected using SISTM visualization^{4,26,32} and X-ray scattering^{26,32,34,35}. It consists of periodic spatial modulations of electronic structure appearing at finite wavevector \mathbf{Q} that occur within the pseudogap phase (Fig. 1A and Methods Section 1). Yet it has been difficult to discern whether the short-range modulations break C_4 symmetry^{41,42}. Critical challenges for this field are thus to identify the correct microscopic theory for the DW state, and to find the relationship (if any) between it and both the NE state and the pseudogap^{26,30,31,33}.

4 Generally, a DW state with wavevector \mathbf{Q} is described by a spatially modulating function $A(\mathbf{r}) = D(\mathbf{r})\cos(\mathbf{Q} \cdot \mathbf{r} + \phi_0(\mathbf{r}))$, where $A(\mathbf{r})$ represents the density amplitude, $\phi_0(\mathbf{r})$ represents effects of disorder and topological defects on the DW spatial phase at location \mathbf{r} . The term $D(\mathbf{r})$ is the DW form factor symmetry which, for a tetragonal

crystal, has *s*-symmetry if it remains unchanged under 90° rotations and *d*-symmetry if changes sign thereby. For the cuprate DW state, $D(\mathbf{r})$ exhibits prevalent *d*-symmetry³⁶⁻⁴⁰. One theoretical approach to understanding a DW state is based on the conventional picture assuming well-defined wave momentum of each electron²⁵. Mobile, weakly correlated electrons each have a definite momentum $\mathbf{p}(E) = \hbar\mathbf{k}(E)$ at energy E , where $|\mathbf{k}(E)| = 2\pi/\lambda(E)$ and $\lambda(E)$ is the electron's quantum wavelength. The set of all possible \mathbf{k} 's for given energy E defines the electronic structure $\mathbf{k}(E)$ in \mathbf{k} -space. The Fermi surface is defined as the \mathbf{k} -space contour $\mathbf{k}(E = 0)$. DW states can then appear at a wavevector $\mathbf{Q} = (\mathbf{k}_i(E = 0) - \mathbf{k}_f(E = 0))$ if many pairs of $(\mathbf{k}_i(0), \mathbf{k}_f(0))$ are connected by the same wavevector \mathbf{Q} , i.e., nested (red arrow Fig. 1B). Under these circumstances, \mathbf{Q} should usually be incommensurate (Fig. 1B and Methods Section 1). An alternative class of theory holds that strongly interacting particle-like electrons may have well-defined position and hence be fully localized in the MI phase, or self-organized into electronic liquid crystal states^{17,18,32} in \mathbf{r} -space. Many such EQM states have been discussed in theory^{17,18,33}, but a typical example exhibits spatially periodic charge density modulations that are crystal-lattice-commensurate, having wavelength $\lambda = 4a_0$ or wavevector $\mathbf{Q} = 2\pi/a_0 (0.25, 0)$ oriented along the Cu-O-Cu axis (Fig. 1C and Methods Section 1). Such lattice-commensurate charge modulations in position-based theories (Fig. 1C) are expected to be robust against changes with electron-density p and electron-energy, while those associated with the geometry of Fermi surface in momentum-based theories (Fig. 1B) are expected to evolve continuously with p .

5 Although it is crucial to discriminate between these position-based or momentum-based theoretic perspectives, this has not been achieved because the cuprate DW state is so profoundly disordered at the nanoscale^{4,32,36,39}. This can be seen directly in a typical image of cuprate electronic structure at $E=\Delta_1$ as shown in Fig. 1D. A fundamental long-term challenge has therefore been to determine if the spatial arrangements of electronic

structure in hole-doped CuO₂ (e.g. Fig. 1E) are lattice-commensurate, unidirectional, with specific wavevectors, or if they evolve continuously with electron-density and electron-energy. The extreme disorder observed in all extensive atomic-scale EQM images^{4,33,36,39}, or concomitantly the broad and fluctuating line-widths detected in reciprocal space^{4,32-39}, have prevented a clear answer to this key question. Indeed, theory shows that conventional Fourier analysis of such noisy and disordered EQM images is fundamentally limited^{41,42} in the valid inference that can be drawn on the exact symmetries of their EQM state.

6 High-data-volume imaging studies of EQM (e.g. Fig. 1E) use SISTM, a technique that allows probabilistic visualization of the density-of-electronic-states $N(\mathbf{r}, E)$ with sub-atomic resolution and crystal-lattice register. The resulting image-array for a given sample is built up from measurements of STM-tip-sample differential electron tunneling conductance $dI/dV(\mathbf{r}, V) \equiv g(\mathbf{r}, V)$ at a square array of locations \mathbf{r} and at a range of tip-sample voltage differences V . All data are acquired at temperatures $1\text{K} < T < 4.2\text{K}$. In theory, $g(\mathbf{r}, V) \propto N(\mathbf{r}, E) / \int_0^{eV_s} N(\mathbf{r}, E') dE'$ for $E = eV$ and V_s is the arbitrary junction-formation bias⁴. Thus, visualization of the spatially-resolved and energy-resolved $N(\mathbf{r}, E)$ – one of the most powerful modern tools for EQM studies – becomes possible. Note that even if $\int_0^{eV_s} N(\mathbf{r}, E') dE'$ is heterogeneous and thus $g(\mathbf{r}, V)$ is not simply related to $N(\mathbf{r}, E)$, the ratio $Z(\mathbf{r}, V) = g(\mathbf{r}, +V)/g(\mathbf{r}, -V)$ may be used as a valid measure of EQM spatial symmetry because the denominators of $g(\mathbf{r}, +V)$ & $g(\mathbf{r}, -V)$ cancel each other. While Fourier analysis of $Z(\mathbf{r}, V)$ to yield $Z(\mathbf{q}, V)$ is an obvious approach to determining the EQM modulation wavevectors, because of the nanoscale spatial disorder (Fig. 1D) the relevant maxima in Fourier reciprocal space (\mathbf{q} -space) are so broad and fluctuate so widely as to be inconclusive. Overall then, the process of going from an array of such $Z(\mathbf{r}, E)$ images (e.g. Fig. 1E) to identifying and understanding the fundamental broken-symmetry state of EQM hidden therein, is highly non-trivial. Moreover, there is typically no established manual scheme of regression to achieve that objective.

7 Development of a ML strategy capable of recognizing hidden EQM ordered states and identifying their broken-symmetries in such image-arrays could be a breakthrough in pinpointing the ordering scenario of EQM states. Although impressive ML-based progress has already been made in the recognition of quantum many-body wavefunctions in synthetically generated EQM data⁵⁻¹⁶, the profound challenge we now face is to develop ML techniques capable of achieving scientific discovery with experimental EQM data sets. Required are general tools for manipulation and analysis of EQM image-arrays, allied with the ability to include human-generated hypotheses into the machine learning process, plus the fundamental capability of ML to identify the key physical phenomena contained in the data. The long-term objectives are to develop a ML strategy capable of recognizing specific EQM states in real (automated, heterogeneous, noisy, incomplete) experimental image-arrays, and to establish reliable functionality of such ML strategies for EQM studies, so that they can become the norm in condensed matter physics labs of the future.

8 Here we introduce a specific ML approach using ANN's to achieve hypothesis testing with EQM image-arrays, based upon supervised ML within an ANN-human coalition. Its goal is to automatically search experimental EQM image-arrays (e.g. Fig. 1E), to recognize spatial modulations in a variety of distinct categories, to identify their fundamental periodicity and lattice register throughout an image, and to distinguish if the modulations are unidirectional or bidirectional. The first stage is to generate the sets of ANN training images, each labeled by a hypothesis: the different DW states to be discerned. Here, we test four hypotheses associated with four distinct types of ideal periodic modulations, all with a d-symmetry form factor, and with fundamental wavevectors $\mathbf{Q}=0.23, 0.25, 0.27, 0.29(2\pi/a_0, 0)$ respectively. Four training sets for categories $C=1, 2, 3, 4$ are then generated using identical procedures, in which we introduce specific forms of heterogeneity designed to mimic the noise, intrinsic disorder and topological defects of

experimental data (Fig. 2A and Methods Section 2). Throughout these simulated training-image-sets, the heterogeneity disrupts the long-range ordered patterns in \mathbf{r} -space as shown for a typical example of a training image in Fig. 2B. It also scrambles the peaks in the d-symmetry Fourier transforms⁴ of the training images, rendering them broad and chaotic (Fig. 2C). In the second stage, we establish an ANN architecture that trains well with these training-image-sets. During training, the parameters of the ANN are adjusted iteratively to minimize a cross-entropy cost function (a measure of the distance between the ANN outcome and the training set label)⁴³. Stochastic gradient descent along with backpropagation⁴⁴ is used for lowering the cost function. The training is complete and all parameters of the ANN are set when the cross-entropy⁴⁵ saturates. Each finalized ANN generally has an accuracy >99% when tested on validation images (Fig. 2D and Methods Section 3). The ANN design is a fully connected feed forward network with a single hidden layer (Fig. 3C and Methods Section 3). Statistical reliability of this ML system against different network architectures and different initial conditions is then achieved by training 82 distinct ANNs in parallel with the same training image-set (Methods Section 3).

9 Our ANN ensemble is then used to hypothesis test the experimental EQM image-array. We first employ the trained ANN's to identify effects of changing the average electron-density within the EQM data. This consists of an array of measured $Z(\mathbf{r}, E)$ electronic-structure images from samples of the hole-doped cuprate $\text{Bi}_2\text{Sr}_2\text{CaCu}_2\text{O}_8$ that span the range of electron density $0.06 \leq p \leq 0.20$. Obviously disorder and complexity of EQM abound in $Z(\mathbf{r}, \Delta_1)$ throughout this whole electron-density range (black double headed arrow in Fig. 1A) and are equally apparent in the broad fluctuating peaks around $(Q_x \pm \delta Q_x, \delta Q_y)2\pi/a_0$ and $(\delta Q_x, Q_y \pm \delta Q_y)2\pi/a_0$ in $Z(\mathbf{q}, \Delta_1)$ (see Figs. 3A,B). One realizes the serious challenge to determine a fundamental modulation wavevector (if extant) in such images because there are no sharp features whatsoever. Indeed, it would appear highly unlikely to human perception that a well-defined DW with a specific modulation-

wavevector could even be hidden therein. The set of measured $Z(\mathbf{r}, E)$ images have FOV 16nmX16nm, but are measured in a sequence of independent experiments on distinct crystals with electron-densities $p \approx 0.06, 0.08, 0.085, 0.20$ ($T_c(K) = 20, 45, 50, 82$). The ANNs analyze these $Z(\mathbf{r}, \Delta_1)$ images as a function of p , focusing on the pseudogap energy $E = \Delta_1(p)$ because cuprate EQM symmetry-breaking emerges at this energy. Figures 4A-D show the actual $Z(\mathbf{r}, \Delta_1)$ images presented to the trained ANN system while Figs. 4E-H show their d -symmetry Fourier transforms. Remarkably, the ANN's succeed with high reliability in discriminating and identifying the key wavevectors throughout these images (Methods Section 4). In Figures 4I-L we show the response of the ANNs as the probability $P(C)$ that the presented EQM image is identified in the category C . Here the ANNs reveal that, on the average, the phenomenology of the $C=2$ training-images has the highest probability of being recognized within the $Z(\mathbf{r}, \Delta_1)$ image-array, but only for electron-densities $p < 0.20$. Thus, when broken translational symmetry exists, it occurs commensurately with the specific wavevector $\mathbf{Q} = (2\pi/4a_0, 0)$ (Fig. 4A-E). Overall, the ANNs conclude that the identical, commensurate, $4a_0$ periodic DW state was hidden throughout the $E \approx \Delta_1$ EQM images from the $p < 20\%$ area of the CuO₂ electronic phase diagram (Fig. 1A).

10 A second key physics issue is the energy dependence within an $Z(\mathbf{r}, E)$ image-array. Quasiparticle scattering interference⁴ (QPI) occurs when an impurity atom scatters wave-like states $\mathbf{k}_i(E)$ into $\mathbf{k}_f(E)$, resulting in quantum inference at wavevectors $\mathbf{Q}_{if}(E) = \mathbf{k}_i(E) - \mathbf{k}_f(E)$, and generating modulations of the density-of-states $\delta N(\mathbf{r}, E)$ or its Fourier transform $\delta N(\mathbf{Q}_{if}, E)$. QPI is a distinct physical phenomenon from a DW state because in the former modulation wavevectors evolve rapidly with electron-energy E while in the latter they are non-dispersive or independent of electron-energy. Therefore, the ANNs explore a Bi₂Sr₂CaCu₂O₈ $Z(\mathbf{r}, E)$ array of 16nmX16nm EQM images, that are measured in a sequence of independent experiments at distinct electron-energy $E = 66, 96, 126, 150$ (meV)

on the same crystal with $p=0.08$. Figures 5A-D show this $Z(\mathbf{r}, E)$ image set that is presented to the same ANN system. EQM complexity in the identical field of view now evolves rapidly with electron-energy because they are dominated by QPI. Similarly, Figures 5E-H are the d -symmetry Fourier transforms $Z(\mathbf{q}, E)$ from Figures 5A-D, showing broad fluctuating peaks around $(Q_x \pm \delta Q_x, \delta Q_y)2\pi/a_0$ and $(\delta Q_x, Q_y \pm \delta Q_y)2\pi/a_0$. But now $\delta Q_x, \delta Q_y$ also evolve rapidly with electron-energy, another quantum mechanical effect expected in QPI. Well-defined fundamental modulation wavevectors appear indiscernible in these $Z(\mathbf{r}, E)$ (A-D); $Z(\mathbf{q}, E)$ (E-H) data. However, Figures 5J-L demonstrate that the ANN suite finds that the hypothesis category with the highest probability of being recognized is again in $C=2$, meaning that the predominant modulations have wavevector $|\mathbf{Q}| = 2\pi/4a_0$ for all energies exceeding 66meV (Fig. 5A-D). Again, despite intense masking by QPI phenomena, the ANN's recognize a commensurate, $4a_0$ periodic, DW state and reveal that its phenomenology arises near the pseudogap energy scale $E = \Delta_1$.

11 A third ANN discovery in Fig. 5I-L is that the commensurate, $4a_0$ periodic modulations exhibit a strong preference for breaking symmetry under 90° rotations (C_4). This is revealed because the ANN array yields up to 3 times higher probability in the specific category ($C=2$) when the data is presented in the X orientation (red) compared to when the identical data is presented to it in the Y orientation (yellow) (Fig. 5I-L). Thus, although the extreme nanoscale disorder prevents this from being discerned in the images Fig. 5A-D, the DW modulations are occurring primarily along the x-axis of the CuO₂ plane. ANN analysis of the energy dependence of this complete $Z(\mathbf{r}, E)$ image array in Fig. 6 further confirms that the appearance of this nematicity (Fig. 5I-L) is at the pseudogap energy scale which is $|\Delta_1| \approx 80\text{meV}$. Thus, the ANNs find that a nematic state emerges at the pseudogap energy, directly because of the extremely disordered yet unidirectional $4a_0$ periodic modulations of the DW. This discovery strongly implies that the nematic electronic

structure of CuO₂ is a vestigial nematic state⁴⁶ whose characteristic energy gap is the pseudogap.

12 Given such an operational ML system for experimental EQM data, one may ask how does ML compare with conventional techniques for such studies? Previous SISTM studies have been made of equivalent phenomena by using Fourier transform (FT) analysis of $Z(r, E)$ images^{4,36,39,40}. But, because of the profound limitations of the FT approach, these studies could firmly establish neither the electron-density dependence of the DW wavevectors nor the relationship between the NE and DW states. Their first limitation is that the Fourier components of any modulations must be preselected prior to analysis, rather than impartially studying each entire $Z(r, E)$ image; this means that what is actually studied using FT techniques is a minute subset of all the information contained in each image. Thus, such heavy pre-processing generates concerns about the objective significance of all FT techniques. By contrast, within the ML approach entire $Z(r, E)$ images are analyzed in a completely unbiased fashion, without wavevector preselection or any other preprocessing (Methods Section 5). Secondly, conventional analysis of every $Z(r, E)$ image requires a skilled researcher, experienced in FT techniques, and the ensuing personnel costs are prohibitive for comprehensive FT studies of the largest experimental data archives. Obviously, ANNs that are efficient at this task would not be so constrained. Thirdly, the linearity of FT renders it incapable of handling predominantly non-linear effects inherent in topological defects such as vortices or edge dislocations within every $Z(r, E)$ image; but such topological defects are critically important in the study of DW states⁴⁷. By contrast, the ML approach is fundamentally based on the non-linearity built into the neural network architecture⁴⁸, and is ideal for encompassing topological defects into its state identification (Methods Section 5). Indeed, one can immediately discern an example of the powerful benefits of these new ML and ANN techniques, in that minute DW correlation lengths make it formally impossible for FT analysis to determine whether the

DW modulations are bidirectional or unidirectional^{41,42}, while the ANN array yields a clearly unidirectional conclusion (Figs 5,6). Advanced theory predicts that a unidirectional DW that is reduced by disorder to extremely short spatial coherent lengths, should generate a nematic state dubbed a vestigial nematic state⁴⁶. Although experimental validation for this hypothesis is formally impossible using FT techniques, here it is demonstrably achievable by an ANN array (Fig. 5,6). Existence of a vestigial nematic state in carrier-doped CuO₂ would provide a direct, internally consistent link between a nematic state and unidirectional $4a_0$ periodic DW modulations, whose energy gap is the pseudogap (Fig. 4).

13 To summarize: we have developed and demonstrated a new general protocol for ML-based identification of the translational symmetry-breaking ordered states in electronic structure image-arrays from EQM visualization experiments. In this human-ANN coalition, traditional human insight into orders and symmetries forms the basis of the training-image generation (Fig. 2). The ANNs are then trained to learn the defining traits of each category (ideal ordered state) including its topological defects and, while processing all data rapidly in an unfiltered and unbiased fashion, to recognize those traits in real EQM image arrays (Fig. 1E). Despite the extreme complexity of the cuprate EQM state, instrument distortion and noise, and the intense electronic disorder of the EQM image arrays studied (Figs.1D,3A,B;4,5), the trained ANNs repeatedly and reliably discover predominant features of a very specific ordered state: a lattice-commensurate, *d*-symmetry form factor, $4a_0$ periodic DW for $p < 20\%$ (Fig. 4). As an advance in CM physics, the predominance of lattice-commensurate DW modulations with wavevector $\mathbf{Q} = (2\pi/4a_0, 0)$ for $p < 0.2$ (Fig. 4) implies that a strong coupling position-based theory is fundamentally required to describe these broken-symmetry states of electron doped CuO₂. Moreover, it indicates that a (quantum) critical point near $p \sim 0.2$ separates this phenomenology from the more conventional wave like states at higher hole density (Fig. 4). Strikingly, the ANN

array also reveals that it is the $\mathbf{Q} = (2\pi/4a_0, 0)$ DW modulations at the pseudogap energy that break the global rotational symmetry to generate a nematic state (Figs. 5,6), thereby unraveling the mystery of how a $\mathbf{Q}=0$ nematic phase could open an energy gap by identifying it as a vestigial nematic⁴⁶. Taken at face value, this implies that the PG region of the phase diagram (Fig. 1A) contains a vestigial nematic state. Concurrently, a milestone for general scientific technique has been achieved with the demonstration that ANN's can process and identify specific broken symmetries of highly complex image-arrays from non-synthetic experimental EQM data, through an ANN-human coalition. Overall, these combined advances open the immediate and exciting prospect of additional ML-driven scientific discovery in EQM studies.

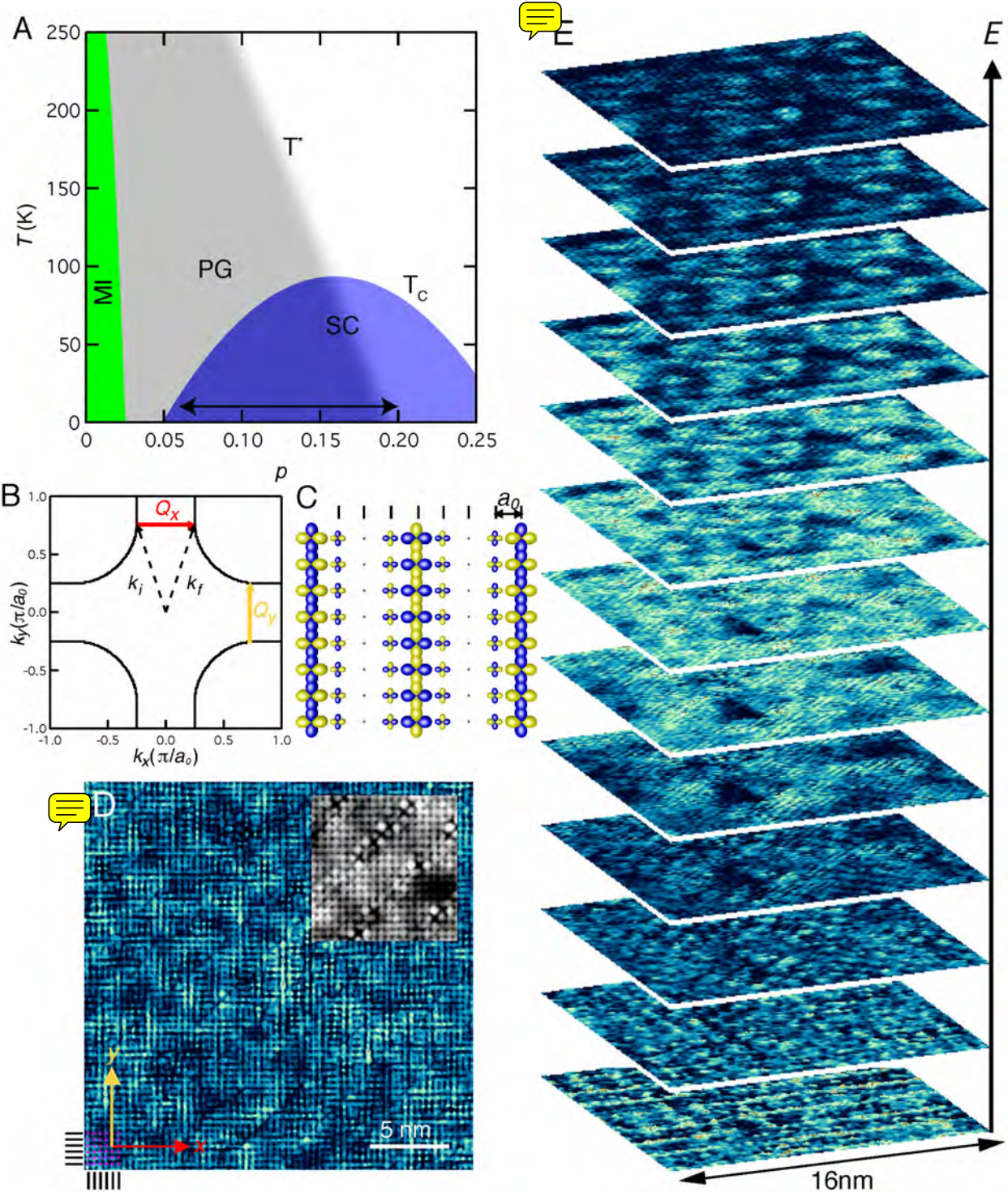


Figure 1. Electronic quantum matter imaging in hole-doped CuO₂. **A**, Schematic phase diagram of hole-doped CuO₂. At $p=0$ a single electron is localized at each Cu site in a Mott insulator (MI) state. As holes are introduced (electrons removed) the MI disappears quickly. The high temperature superconductivity (SC) emerges at slightly higher p , reaching its maximum critical temperature T_c near $p\sim 0.16$. However, in the range $p<0.2$ and up to temperatures T^* an enigmatic phase of EQM, dubbed the pseudogap (PG) phase, is known to contain periodic charge density modulations of imprecise wavevector \mathbf{Q} . **B**, In the CuO₂ Brillouin zone, the Fermi surface is defined as the k -space contour $\mathbf{k}(E = 0)$ that separates the occupied from unoccupied electronic states, and its locus changes rapidly with changing carrier density p . Density wave (DW) states may then appear at a wavevector $\mathbf{Q}(\mathbf{k}_i(E = 0) - \mathbf{k}_f(E = 0))$ if the electron states $\mathbf{k}_i(E)$ and $\mathbf{k}_f(E)$ are "nested" (red and yellow arrows). **C**, Strongly correlated electrons may be fully localized in the Mott insulator phase, or self-organized into electronic liquid crystal states^{17,32} in r -space. Schematically shown here is a simple example of a state with unidirectional charge density modulations in the CuO₂ plane, having wavelength $\lambda = 4a_0$ or wavevector $\mathbf{Q} = \frac{2\pi}{a_0}(0.25, 0)$ (Methods section 1). **D**, Typical 24.4nmX24.4nm SISTM image of electronic structure $R(r, E = 150mV)$ from the CuO₂ plane of Bi₂Sr₂CaCu₂O₈ with $p=0.08$ ($T_c=45K$). Complex spatial patterns, which to human visual perception look like highly disordered "tweed", dominate. The contrast with simple periodic arrangement of the simultaneously visualized atoms of the same crystal in the topograph (upper inset) is arresting. **E**, Typical image-array of simultaneously measured $Z(r, E)$ for $p=0.08$, each 16nmX16nm but at a different electron energy E , spanning the range $6meV < E < 150meV$ in steps of 12 meV. Such arrays are the basic type of data-set for which efficient ML analysis and discovery techniques are urgently needed.

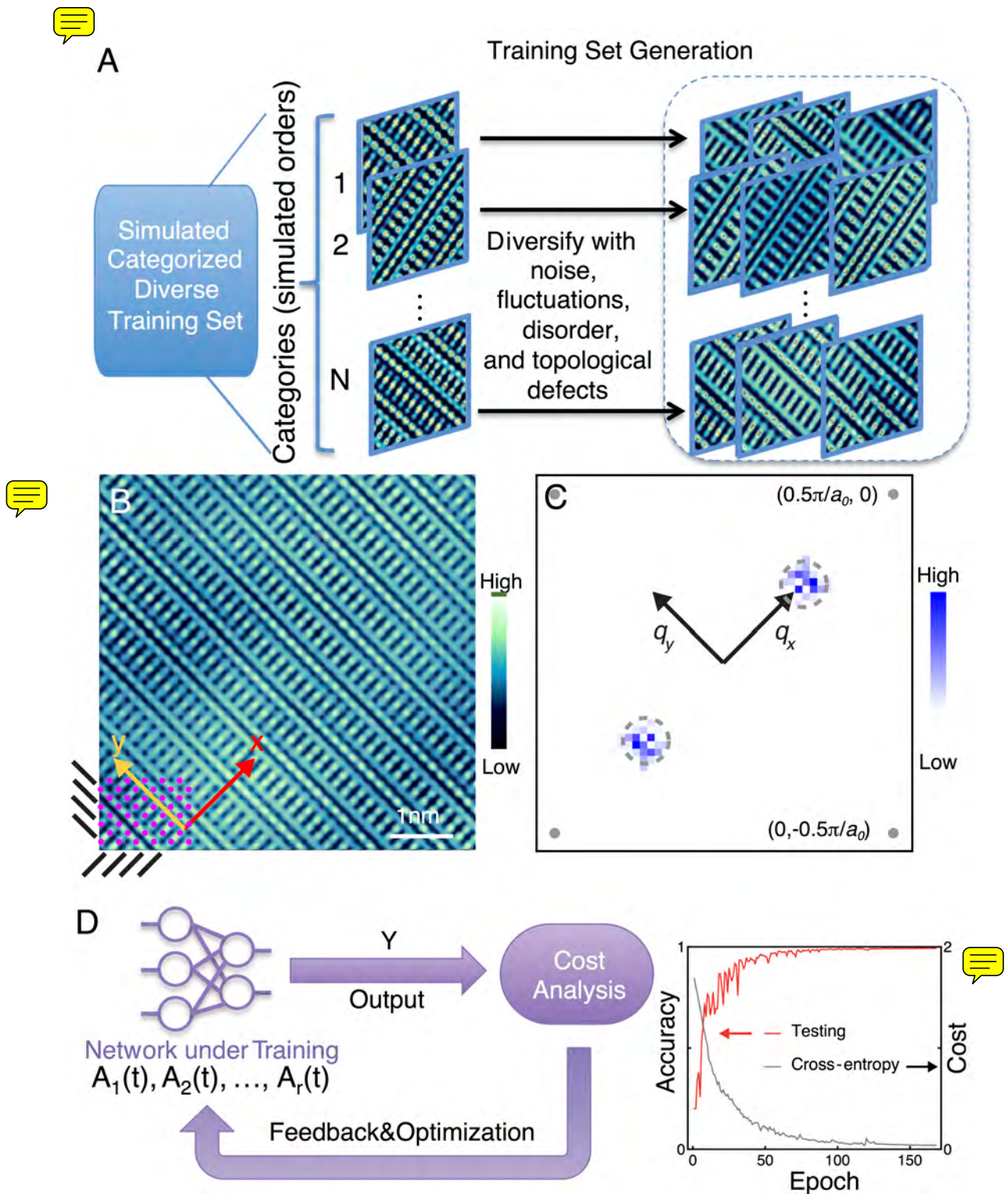


Figure 2. Training ANN to identify broken-symmetry states in SISTM data. **A**, The ANN array is trained to recognize a DW in electronic structure images (e.g. $Z(\mathbf{r}, E)$) representing different EQM states. A synthesized training-image set for the ANNs is obtained by appropriately diversifying pristine images of 4 distinct electronic ordered states. Each translational symmetry-breaking ordered state is labeled by a category $C = 1,2,3,4$ associated with its wavevector: $Q_C = 0.23, 0.25, 0.27, 0.29 (\frac{2\pi}{a_0}, 0)$ respectively. The training-images in each category are diversified by appropriate addition of noise, short correlation-length fluctuations in amplitude and phase, and topological defects. **B**, Example of a training-image in category $C=2$ which is a d -symmetry form factor (dFF) DW with $Q = 0.25 (\frac{2\pi}{a_0}, 0)$ within which smooth amplitude and phase fluctuations and randomized positions of topological defects (dislocations) have been added to simulate typical phenomena encountered in experimental EQM visualization (e.g. 1D). The full 516x516 pixel image contains 2x86x86 entire CuO₂ unit-cells with Cu-Cu distance of 6 pixels diagonally. **C**, The d -symmetry Fourier transform of **B**. Absence of a well-defined modulation wavevector Q within the modulations in **B** has been successfully simulated in the training-image as seen by the region of q -space (grey dashed circle) within which strong variation in the amplitudes at different wavevectors occur. Grey dots are at $q = \left[\frac{2\pi}{a_0} \right] (\pm 0.5, 0); (0, \pm 0.5)$. **D**, Each ANN is trained by minimizing the cross-entropy cost function progressively through stochastic gradient descent and back propagation. The process of going through the entire set of shuffled training data, also known as an epoch, is repeated until the cross-entropy and accuracy saturate. The overall accuracy of the finalized ANNs on the synthesized data is generally over 99%.

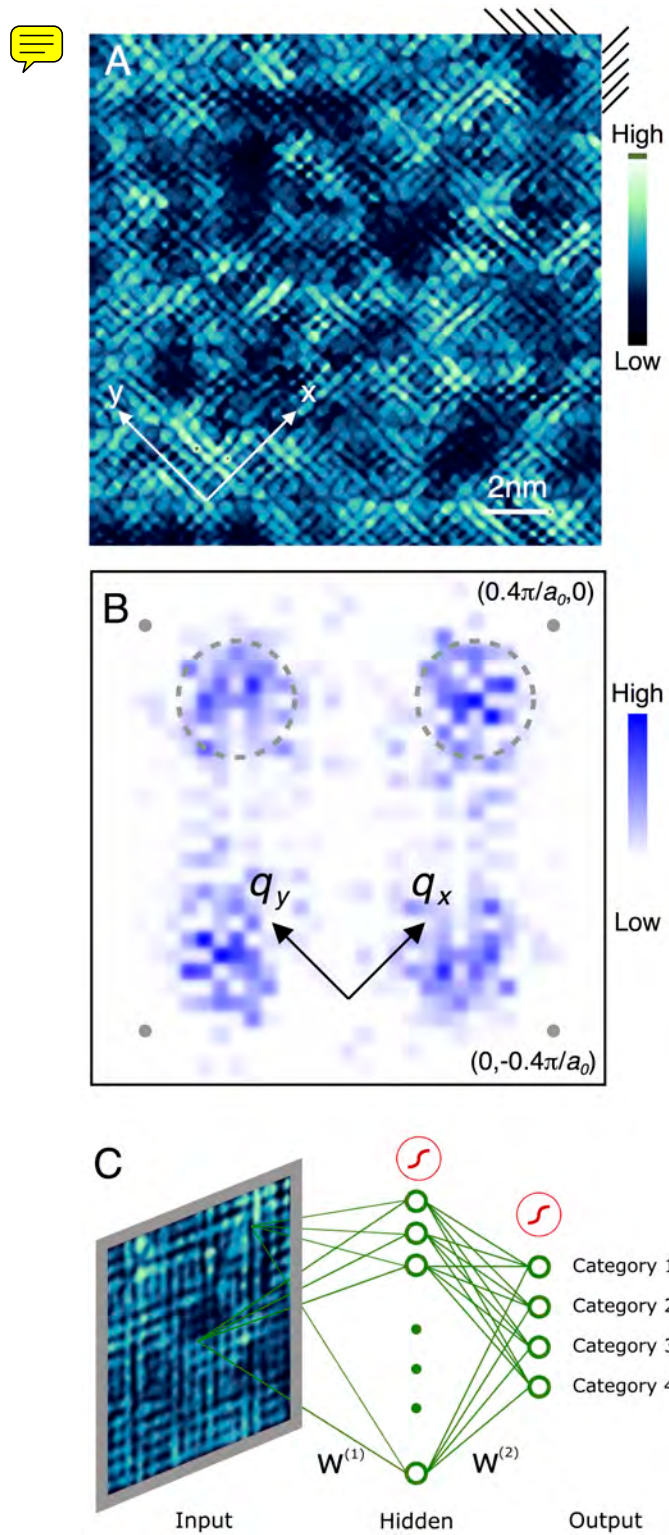


Figure 3. ANN analysis of experimental EQM visualization data. **A**, Typical measured 16nmX16nm $Z(\mathbf{r}, E = 84\text{meV})$ image of $\text{Bi}_2\text{Sr}_2\text{CaCu}_2\text{O}_8$ with $p=0.08$ ($T_c=45\text{K}$). The disorder and complexity of EQM are vivid. **B**, Typical measured $Z(\mathbf{q}, E = 84\text{meV})$ image of $\text{Bi}_2\text{Sr}_2\text{CaCu}_2\text{O}_8$ with $p=0.08$ ($T_c=45\text{K}$) being the d-symmetry Fourier transform of **A**. The disorder and complexity of EQM are equally vivid here in the broad and fluctuating peaks around $(Q_x \pm \delta Q_x, \delta Q_y)2\pi/a_0$ and $(\delta Q_x, Q_y \pm \delta Q_y)2\pi/a_0$ with $|\delta Q_x| = |\delta Q_y| \approx 0.2$. Grey dots are at the $(0.4,0); (0,0.4)2\pi/a_0$ points. **C**, Schematic of ANN analysis procedure for experimental $Z(\mathbf{r}, E)$ images: the successfully trained neural network with fixed parameters (weights $W^{(1)}$ and $W^{(2)}$ of the hidden layer and the output layer respectively and biases) is a classifier: It classifies each experimental image as belonging into one of the four categories. Neuron activation functions in our ANNs are taken to be the sigmoid function.

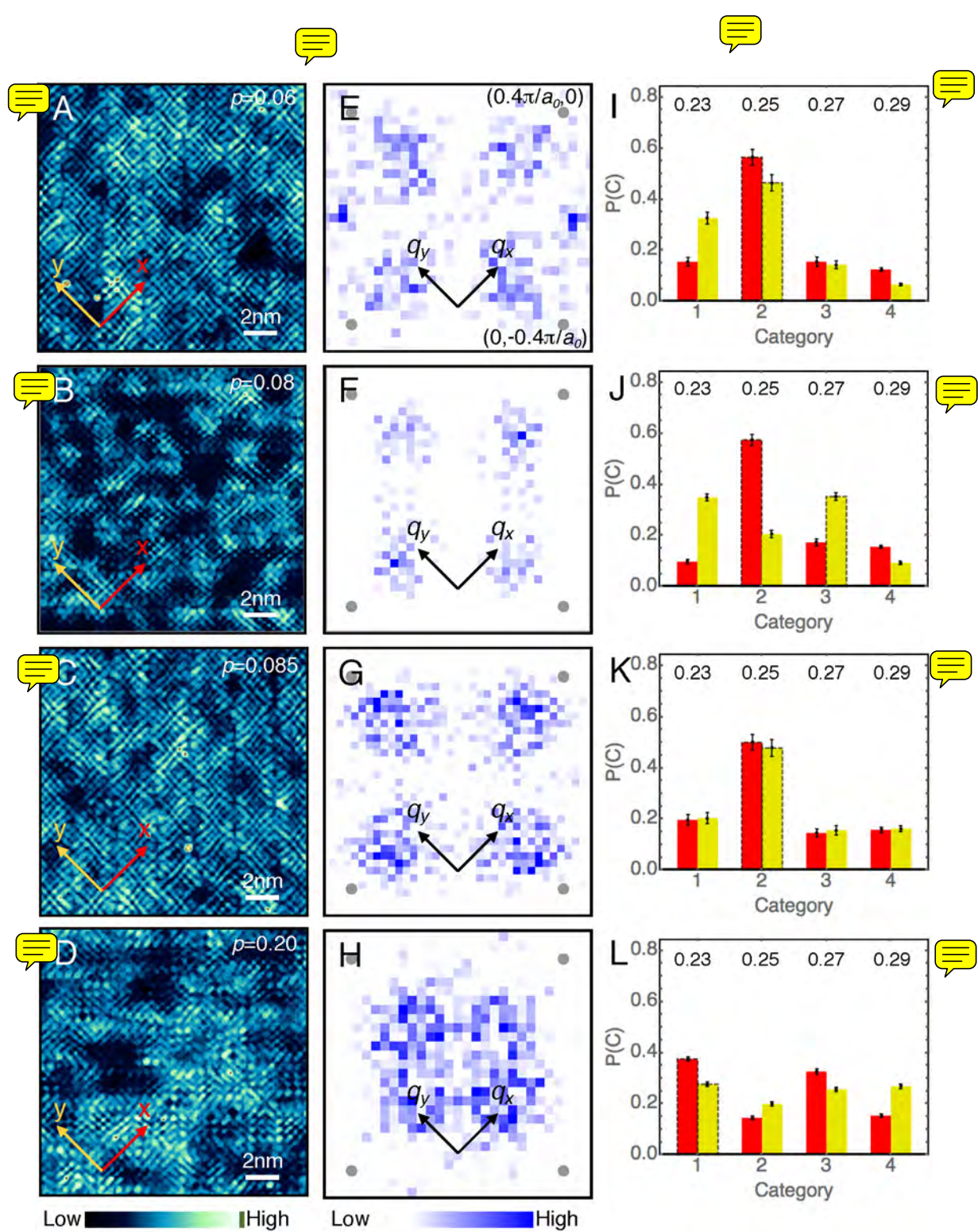


Figure 4. ANN detection of broken-symmetry evolution with electron-density. **A-D**, Measured 16nmX16nm $Z(\mathbf{r}, E)$ images of $\text{Bi}_2\text{Sr}_2\text{CaCu}_2\text{O}_8$ in a range of electron densities with $p=0.06, 0.08, 0.085, 0.20$ ($T_c(\text{K})=20, 45, 50, 82$). Each image is measured at $E = \Delta_1(p)$ the pseudogap energy at that electron-density. Obviously disorder and complexity of cuprate EQM abound throughout this whole electron-density range (black double headed arrow in Fig. 1A). **E-H**, The d -symmetry Fourier transforms $Z(\mathbf{q}, E)$ from **A-D**. The disorder and complexity of EQM are equally vivid as broad fluctuating peaks around $(Q_x \pm \delta Q_x, \delta Q_y)2\pi/a_0$ and $(\delta Q_x, Q_y \pm \delta Q_y)2\pi/a_0$. Grey dots are at the $(0.4, 0); (0, 0.4)2\pi/a_0$ points. **I-L**, Output categorization by 82 ANNs of the preprocessed images from **A-D**. Top row numbers: the length of category's fundamental wavevector, in units of $\frac{2\pi}{a_0}$. We take statistics of independent assessment on the given experimental image by 82 ANN's that are independently trained to arrive at the probabilities $P(C)$ of the image belonging to category C . The error bars mark the uncertainty (one standard deviation) of the averaged value of the ANN outputs, as estimated from our ensemble of 82 ANN realizations (see Methods). Since the training-images for ANNs are unidirectional, i.e., their pristine orders have wavevectors $\vec{Q}_C = Q_C \vec{e}_x$, categorization results for two modulation orientations X,Y (red and yellow bars) are obtained by inputting to ANNs the preprocessed $Z(\mathbf{r}, E)$ images and their 90-degree rotated versions, respectively.

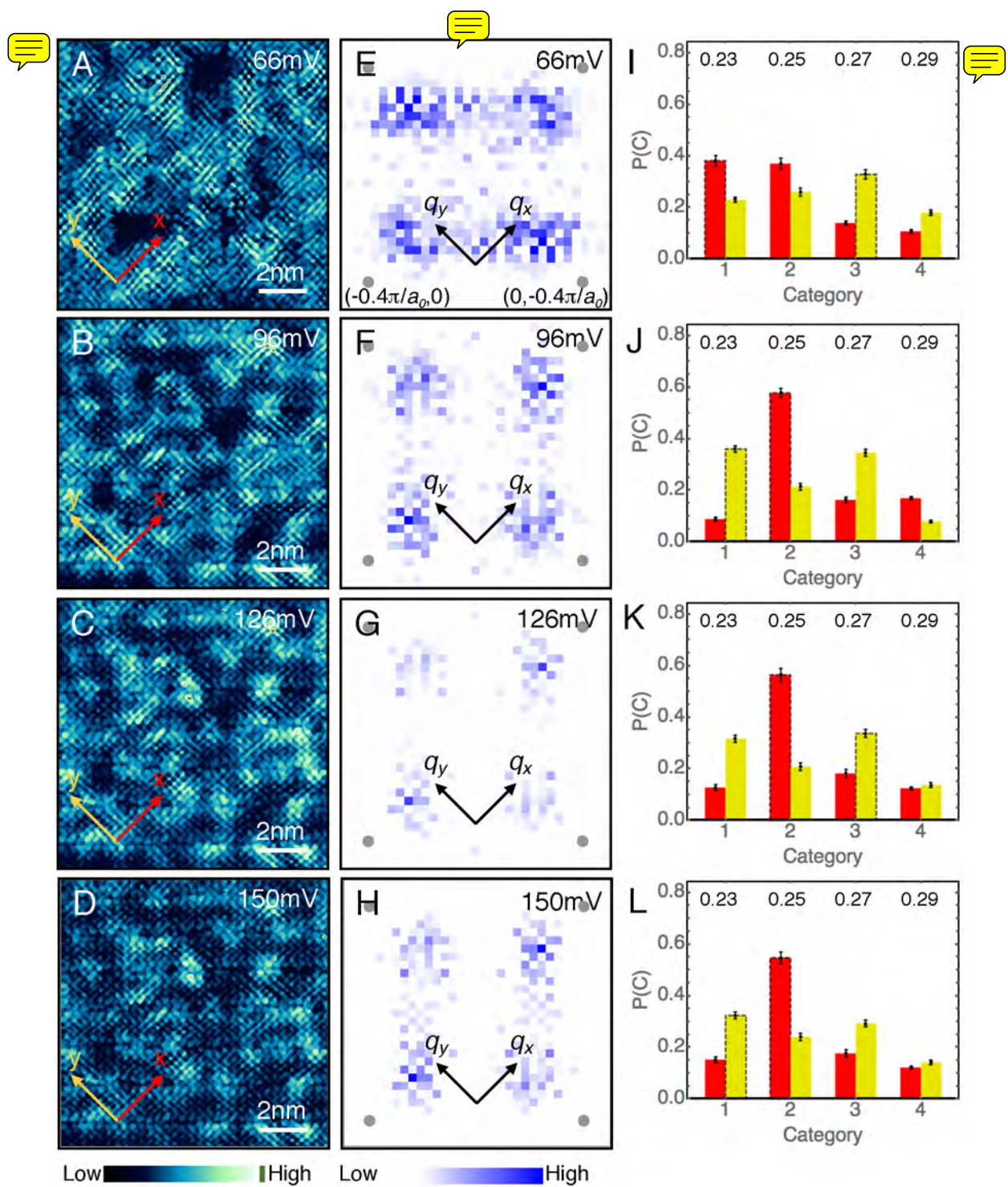


Figure 5. ANN detection of broken-symmetry at different electron-energies. A-D, Measured 16nmX16nm $Z(\mathbf{r}, E)$ images of $\text{Bi}_2\text{Sr}_2\text{CaCu}_2\text{O}_8$ in a range of electron-energy $E=66, 96, 126, 150$ (meV) for $p=0.08$ ($T_c(\text{K})=45\text{K}$). EQM complexity in the identical field of view, now evolves rapidly with electron-energy, a purely quantum mechanical effect. **E-H**, The d -symmetry Fourier transforms $Z(\mathbf{q}, E)$ from **A-D**. The disorder and complexity of EQM are strong as seen in the broad fluctuating peaks around $(Q_x \pm \delta Q_x, \delta Q_y)2\pi/a_0$ and $(\delta Q_x, Q_y \pm \delta Q_y)2\pi/a_0$ but now $\delta Q_x, \delta Q_y$ evolve rapidly with electron-energy (another quantum mechanical effect). Grey dots occur at $(0.4, 0); (0, 0.4)2\pi/a_0$ points. **I-L**, Output categorization by 82 ANNs of the preprocessed images from **A-D**. Top row numbers: the length of category's fundamental wavector, in units of $\frac{2\pi}{a_0}$. We take statistics of independent assessment on the given experimental image by 82 ANN's that are independently trained to arrive at the probabilities $P(C)$ of the image belonging to category C. The error bars mark the uncertainty (one standard deviation) of the averaged value of the ANN outputs, as estimated from our ensemble of 82 ANN realizations (see Methods). Categorization results for two modulation orientations X,Y (red and yellow bars) are obtained by inputting to ANNs the preprocessed $Z(\mathbf{r}, E)$ image-array and its 90-degree rotated version, respectively.

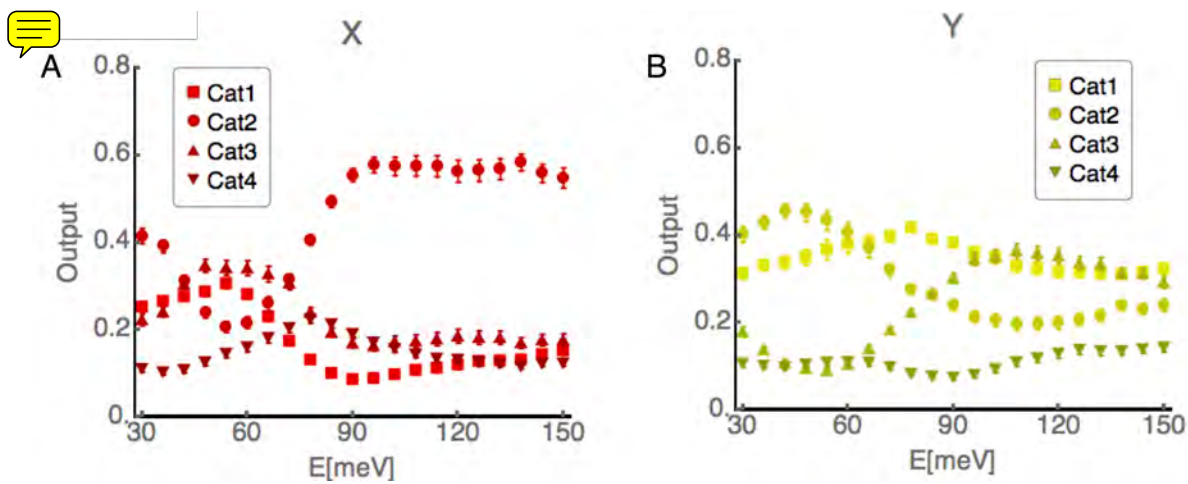


Figure 6. ANN detection of unidirectionality at different electron-energies. **A, B,** Output categorization by 82 ANNs of the preprocessed 16nmX16nm $Z(\mathbf{r}, E)$ images of $\text{Bi}_2\text{Sr}_2\text{CaCu}_2\text{O}_8$ in a range of electron-energy $E=30\dots150$ (meV) in steps of 12 meV for $p=0.08$ (T_c (K)=45K). The error bars mark the uncertainty (one standard deviation) of the averaged value of the ANN outputs, as estimated from our ensemble of 82 ANN realizations (see Methods). **A**, Output for modulation orientation X is obtained by inputting to ANNs the preprocessed $Z(\mathbf{r}, E)$ image-array. **B**, Output for modulation orientation Y is obtained by inputting to ANNs the 90-degree rotated versions of the preprocessed used for **A**.

Acknowledgements

We thank Paul Ginsparg, Jenny Hoffman, Steve Kivelson, Andy Millis, Roger Melko, Miles Stoudenmire, Kilian Weinberger, Jan Zaanen for helpful discussions and communications. E.-A.K., A.M., and Y.Z. acknowledge support from DOE DE-SC0010313; E.-A.K. and Y.Z. acknowledge support from DOE DE-SC0018946; S.U. and H.E. acknowledge support from a Grant-in-aid for Scientific Research from the Ministry of Science and Education (Japan) and the Global Centers of Excellence Program for Japan Society for the Promotion of Science. E.K. and K.C. acknowledge support from the NSF Grant No. DMR-1609560. E.-A.K. and E.K. acknowledge support from the Kavli Institute for Theoretical Physics, supported in part by the NSF under Grant No. PHY-1748958, where initial discussions about the project took place. K.F. and J.C.S.D. acknowledge support from the U.S. Department of Energy, Office of Basic Energy Sciences, under contract number DEAC02-98CH10886. S.D.E, M.H.H and J.C.S.D. acknowledge support from the Moore Foundation's EPiQS Initiative through Grant GBMF4544. J.C.S.D. acknowledges the hospitality of Tyndall National Institute, University College Cork, IRL.

Author Information Reprints and permissions information is available at www.nature.com/reprints. The authors declare no competing financial interests. Readers are welcome to comment on the online version of the paper. Correspondence and requests for materials should be addressed to E.-A. K.; eun-ah.kim@cornell.edu

METHODS

1 Strong coupling density wave states. Position-based strong coupling theories for carried doped CuO₂ predict lattice commensurate, unidirectional, density waves in various electronic degrees of freedom. Among them are two candidate states that can both lead to $4a_0$ -periodic modulations of the charge density and of the local density of states $N(\mathbf{r})$ with wavevector $\mathbf{Q} = (2\pi/4a_0, 0)$. First, a $4a_0$ -periodic modulation in the charge density on the two oxygen sites O_x and O_y within each unit cell but with a relative phase π between them. This is a d-symmetry form factor charge density wave existing as a fundamental ordered state. Second, an $8a_0$ -periodic modulation of *d*-wave Cooper pair density can exist as a fundamental ordered state, ant it induces a $4a_0$ -periodic modulation in the charge density. These two distinct fundamental states are shown schematically in Extended Data Fig.1a,b respectively.

2 Training image set generation. The diversification of synthetic images of a unidirectional DW to create a training image set (see Extended Data Fig.2) starts from d-wave and s-wave form factor (DFF and SFF) components, and includes (1) heterogeneity through independent amplitude and phase fluctuations and (2) topological defects or dislocations in DFF. For any of the C=1,2,3,4 categories with representative wave number Q_C , the DFF ($I_{C,f,d}^{DFF}$) and SFF (I_f^{SFF})form factor modulations with noise models were

$$I_{C,f,d}^{DFF}(x,y) = A_{DFF} [1 + \varepsilon_A A_f(x,y)] A_d(x,y) \cos(Q_C x + \varepsilon_\varphi \varphi_f(x,y) + \varphi_d(x,y) + \varphi_{DFF}),$$

$$I_f^{SFF}(x,y) = A_{SFF} [1 + \varepsilon_A A_f(x,y)] \cos(\varepsilon_\varphi \varphi_f(x,y) + \varphi_{SFF}), \quad (\text{S1})$$

with overall constants $A_{DFF}=1$, $A_{SFF}=0.5$ and phase offsets $\varphi_{DFF} = \pi/4$, $\varphi_{SFF} = 0$. Here the amplitude field $A_f(x,y)$ and the phase field $\varphi_f(x,y)$ field capture smooth fluctuations

(different random realizations in $I_{C,f,d}^{DFF}(x,y)$ and $I_f^{SFF}(x,y)$), and $A_d(x,y)$, $\varphi_d(x,y)$ capture dislocation defects. For each category, we generate different realizations labeled by f and d . For each realization f the $A_f(x,y)$ field is two-dimensional Gaussian fluctuation field with spatial length scale $\xi_A=8a$, normalized between (-1) and 1, while $\varphi_f(x,y)$ is two-dimensional Gaussian fluctuation field with the same spatial lengthscale $\xi_\varphi=8a$, normalized between $-\pi$ and π . The values of correlation lengthscales ξ_A , ξ_φ are motivated by a simple analysis of an SI-STM $Z(\mathbf{q}, E)$ Fourier transform (Fig. 3). The strengths of amplitude and phase fluctuations $\varepsilon_A=0.8$, $\varepsilon_\varphi=0.5$ are also chosen to produce images in rough consistency with a typical $Z(\mathbf{r}, E)$. In each image, there are $n_d=2$ dislocations at random positions $\mathbf{x}_i=(x_i, y_i)$, $i=1 \dots n_d$, with windings $w_i=\pm 2\pi$ and total winding 0. The total dislocation-contributed fields are:

$$A_d(\mathbf{x}) = \prod_{i=1}^{n_d} (1 - \exp(-|\mathbf{x} - \mathbf{x}_i|/\xi_d))$$

$$\varphi_d(x, y) = \sum_{j=1}^{n_d} \text{Arg}[\text{sgn}(w_j)(x - x_j) + i(y - y_j)],$$

where the amplitude recovery length is $\xi_d=a$, motivated by $Z(\mathbf{r}, E)$.

Then the training set for each category C combines the different form factor components into image intensity at pixel position (x,y) in units of a through

$$I_C(x, y) = I_{C,DFF}(x, y) * D(x, y) + I_{C,SFF}(x, y) * S(x, y),$$

using atomic masks: the SFF mask $S(x,y)$ is a sum of two-dimensional Gaussians with maxima equal to one and spatial widths equal to $0.35a$, each located at a Cu atom position (x,y integer), while the DFF mask $D(x,y)$ is a sum of positive Gaussians at locations of O_x and negative ones at O_y 's. The total intensity $I_C(x,y)$ of all simulated images is normalized to take values between 0 and 1. All simulated images have 6 pixels per nearest Cu-Cu distance a , and contain 2x86x86 unit-cells, for the total size of 516x516pixels.

3 Configuration of Artificial Neural Network (ANN). In a feed-forward fully-

connected artificial neural network, the neurons form a layered structure and the output of each neuron is sent to all the neurons in the subsequent layer. Each neuron assesses all the inputs with a series of weights \mathbf{w} , and an additive constant b known as the bias, and determines the output through a non-linear transformation $f(\mathbf{w} \cdot \mathbf{x} + b)$, called the activation function. The bias b and the weights \mathbf{w} , are the parameters of the ANN and adjusted during the training. The activation function usually takes the form of the sigmoid function or the rectified linear unit, see the inset of Extended Data Fig.3a. We also use a softmax function $\sigma(\mathbf{x})_j = e^{x_j} / \sum_j e^{x_j}$ for the output layer to normalize the output and allow a probabilistic interpretation for the different categories.

For supervised machine learning, we divide the data set into a training set containing 90% of the images and the rest 10% for unbiased validation, speed control, and overfitting detection during the training. The weights and biases of the ANN are optimized using stochastic gradient descent to minimize the cross-entropy cost function:

$$C = \frac{1}{N} \sum_{\mathbf{x}} \sum_{i=1}^4 [y_i \ln(\sigma_i) + (1 - y_i) \ln(1 - \sigma_i)],$$

where y_i and σ_i are, respectively, the desired output consistent with the label and the actual ANN output for each of the input image data \mathbf{x} . We use a batch size of 50, and L2 regularization to avoid overfitting. We include 50 neurons in the hidden layer and choose the sigmoid function as the neuron activation function unless stated otherwise. In Extended Data Fig.3a we show examples of the cost function as well as the accuracy on the validation data set for both choices of the sigmoid and the ReLU activation functions during the training. Extended Data Fig.3b shows the achieved accuracy and cross-entropy cost after 25 epochs as a function of the number of neurons in the single hidden layer. We have trained 82 ANNs with random initial conditions by using a stochastic training process. The outputs of the finalized ANNs are robust and quantitatively consistent with each other. Our results in the main text show the average and standard deviations from all 82 ANNs.

To verify that our results are robust against changes to the architecture of the ANN, we have trained 6 ANNs with 100 neurons in the single hidden layer, and 6 ANNs with two hidden layers, and we found that the results agree with each other within error bars.

Because they are drawn from a historic image-array archive not designed for ML based studies, the SI-STM image-arrays $Z(\mathbf{r}, E)$ vary in spatial resolution from sample to sample from 1.7 to 11.5 pixels per a , the average *Cu-Cu* distance. The number of CuO_2 unit-cells in experimental images also varies from 2x55x55 to 2x175x175. The *Cu* and O_{xy} atom positions, registered from the topograph, show random distortions of the lattice due to the STM tip drift effect (Extended Data Fig.4a).

To correct for the drift and standardize all the $Z(\mathbf{r}, E)$, we preprocess each $Z(\mathbf{r}, E)$: (1) using interpolation we map the $Z(\mathbf{r}, E)$ to the resulting input image, in a way that each topographic atom position maps onto a position in a perfect atomic lattice with *Cu-Cu* distance of $a=6$ pixels (see Extended data Fig.4b,c), which corrects both the drift effect and standardizes the spatial resolution; (2) we crop or tile the image to size 516x516pixels; (3) to study the degree of unidirectionality, for each input image we create a copy rotated by 90°, since the training images have modulations only along X direction for simplicity and clarity. An example *Mathematica* notebook file for preprocessing is available. Extended Data Fig.5 shows the $Z(\mathbf{r}, E)$ and their preprocessed images for BSCCO at different dopings. It should be noted that the results are reliable only if the test data lie reasonably consistently within the input space given by the synthetic training sets.

4 Validation and Benchmarking. To assess the discriminatory power of ANNs' categorization, we study obvious modulations in two experimental images (Extended Data Fig.6): (1) Topograph of BSCCO, which has no human-discriminable modulation except for the *Cu* atomic lattice (an SFF at $Q=0$); (2) $Z(\mathbf{r}, E)$ of NCCOC, with obvious commensurate period $4a_0$ modulations, apparent in a DFF Fourier transform. The ANNs' categorization is in full accord.

We also checked the robustness of our approach against existence of superlattice modulations. The assessment of the ANN's were independent of existence or absence (data with superlattice modulation removed from Fourier Transform) of the superlattice modulations.

We further tested the robustness of the ANN decisions against the change in the disorder model. For this we trained a new ANN with the training set generated with different disorder parameters. Specifically, we decreased the amplitude fluctuation intensity ε_A by 13%, and phase fluctuation intensity ε_φ by 20%, while making the disorder profiles vary more rapidly in space by decreasing the correlation lengths ξ_A , ξ_φ by 6%.

Repeating the assessment of experimental data shown in Fig.4I,J,K,L and Fig.6A with the new ANN, we find the results remain unchanged. This is shown through the comparison between the reprint of Fig.4I,J,K,L and Fig.6A here as Extended Data Fig.7A-E respectively and the output from the ANN trained with the new disorder model as Extended Data Fig.7F-J. Robust observations are 1) preference for the commensurate period $4a_0$ for systems with $p < 0.2$ (Extended Data Fig.7A-D, and F-I) and complete confusion over different candidate categories for $p > 0.2$ (Extended Data Fig.7E and J). The energy dependence comparison between the ANN's assessments in the main text (Fig.6A or Extended Data Fig.7E) and the assessments of the ANN trained with the altered disorder model (Extended Data Fig.7J) shows that the tie between the onset of preference for the commensurate period $4a_0$ and the nematicity at the pseudogap energy scale is equally robust against variations in the disorder model used to train ANN's.

5 Comparison between FT-based and ANN-based approach to DW Detection. The Fourier transform(FT) based linear analysis of equivalent data in Ref. 40 was carried out using the fact that the power spectral density is not smoothly distributed (Extended Data Fig.8a,b, reproduced from the SI of Ref. 40.). We had introduced the concept of demodulation residue (DR), using

$$\mathbf{R}_q^\alpha[\psi] \equiv \int \frac{d^2x}{L^2} \text{Re}[\Psi_q^*(\mathbf{x})(-i\partial_\alpha)\Psi_q(\mathbf{x})],$$

$\alpha = x, y$, which measures the phase fitness of the \mathbf{q} -modulation in spatial pattern $\psi(\mathbf{r})$ through filtered FT:

$$\Psi_q(\mathbf{k}) = \exp\left(-\frac{(\mathbf{k}-\mathbf{q})^2}{2\Lambda^2}\right) \exp(-i \mathbf{q} \cdot \mathbf{x}) \tilde{\psi}(\mathbf{q} + \mathbf{k}), \quad (\text{S2})$$

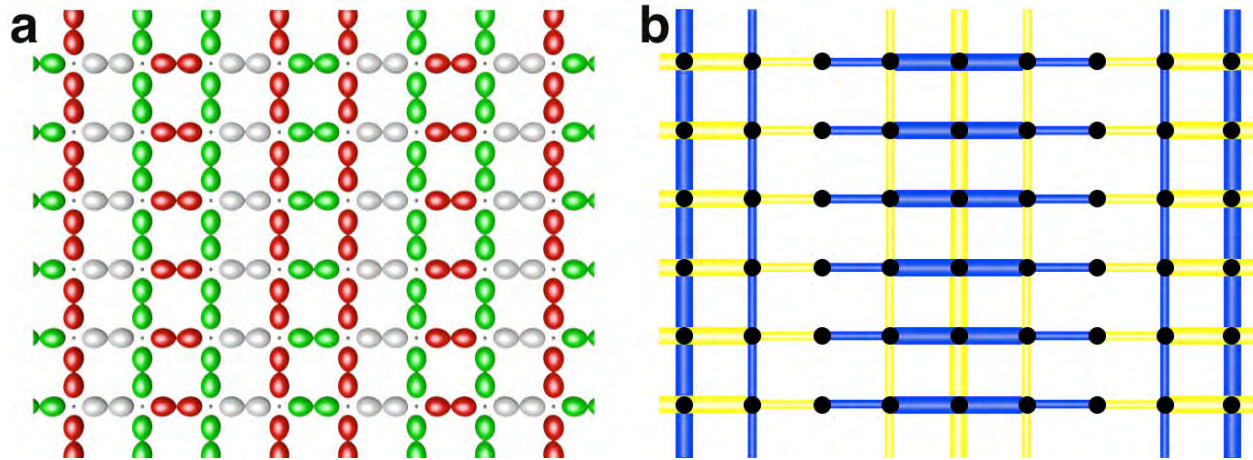
where $\tilde{\psi}(\mathbf{k})$ is the FT of the data. By minimizing the DR, $R_q[\psi] \equiv \sqrt{\mathbf{R}_q^x[\psi]^2 + \mathbf{R}_q^y[\psi]^2}$, for a given modulation while considering different \mathbf{q} -modulations, we showed that one can obtain the phase averaged wave vector $\bar{\mathbf{Q}}$ of DW modulations. Within the limits of Fourier transform, which is a linear basis transform, this approach was an advancement in dealing with situations when the amplitude does not show well defined peaks, due to severe disorder.

However there are severe deficiencies in this approach because FT is a linear transformation of basis and is useful when the desired phenomenon has sharp features in the new basis: the wave-vector basis. However, when there are randomly placed patches of a real-space DW pattern with sprinkles of topological defects, Fourier transform based methods perform very poorly. Obviously, one would not attempt a Fourier transform in trying to recognize human faces in an image for precisely this reason. The limitation of the FT-based methods is evident in that, even when a modulation pattern consists of commensurate period $4a_0$ modulation ($Q_0=2\pi/4a_0$) everywhere except for a sequence of discommensurations (phase slips in commensurate modulation pattern), the $R_q[\psi]$ minimization (as well as the FT amplitude maximization) incorrectly identifies an apparent period of $\bar{Q}=0.3*2\pi/a_0$ (Extended Data Fig.8E). Although in Ref. 40 the DR minimization yielded $\bar{Q} = 2\pi/4a_0$ for pseudogap energy data (single data set for each doping) for various dopings, this depended critically on human visual inspection to identify commensurate patches in Fig. S6B of Ref. 40. Furthermore, the DR based approach therein averaged over topological defects (dislocations) ignoring their profoundly significant role. Finally, the DR based approach required manual choice of Fourier cutoff (Λ in Eq.S2) again based on

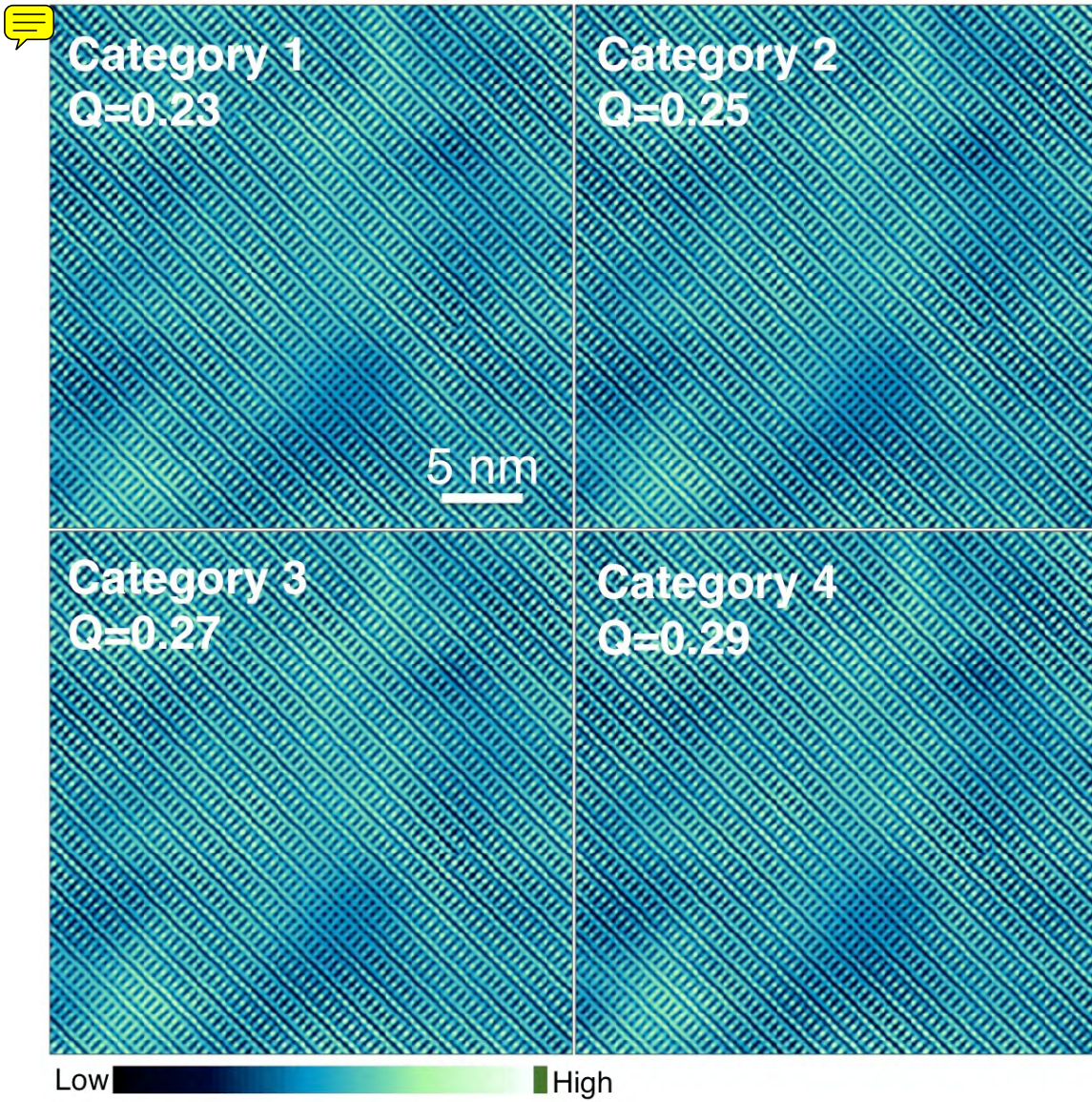
human visual inspection of the data. Hence the entire process is time consuming and high-level human labor intensive and fraught with human perceptual bias. It is therefore not possible to study the largest SISTM image-arrays with this FT approach in any consistent way, rendering it impossible to inspect the complete electron-density and electron-energy dependence of the largest EQM image-array archives.

The ANN-based approach we introduce in the main text is far more powerful, efficient and general. It does not rely on arbitrary choices such as cut-off Λ , or on visual selection of Fourier regions of interest, and is not tied to any basis. The ANN is inherently non-linear and an ANN with sufficient number of neurons can express/detect any function.⁴⁸ Due to the versatility of ANN's, our ANN-based approach allows us to rapidly analyze a complete image-array data set in its entirety, without any ad-hoc Fourier filtering or selection. Hence the ANN approach is quite unbiased. Moreover, once the ANN's are trained, the automatic assessment of new data set takes minutes, allowing for a high-throughput analysis. It is this efficiency that allowed discovery of the connection between nematic state and commensurate density wave state, both setting in at the pseudogap energy scale (Fig.6).

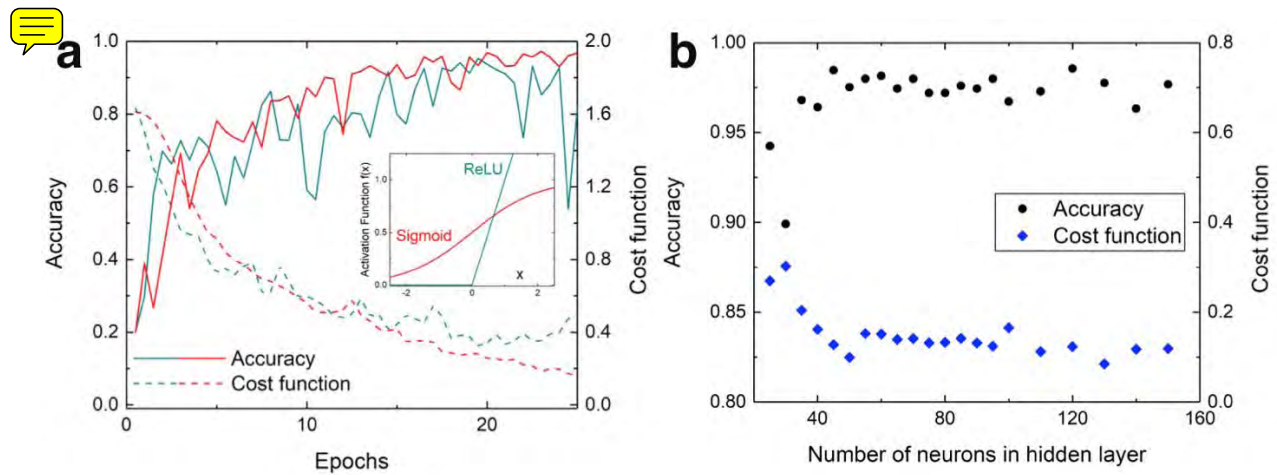
Data Availability The data that support the findings of this study are available from the corresponding author upon reasonable request.



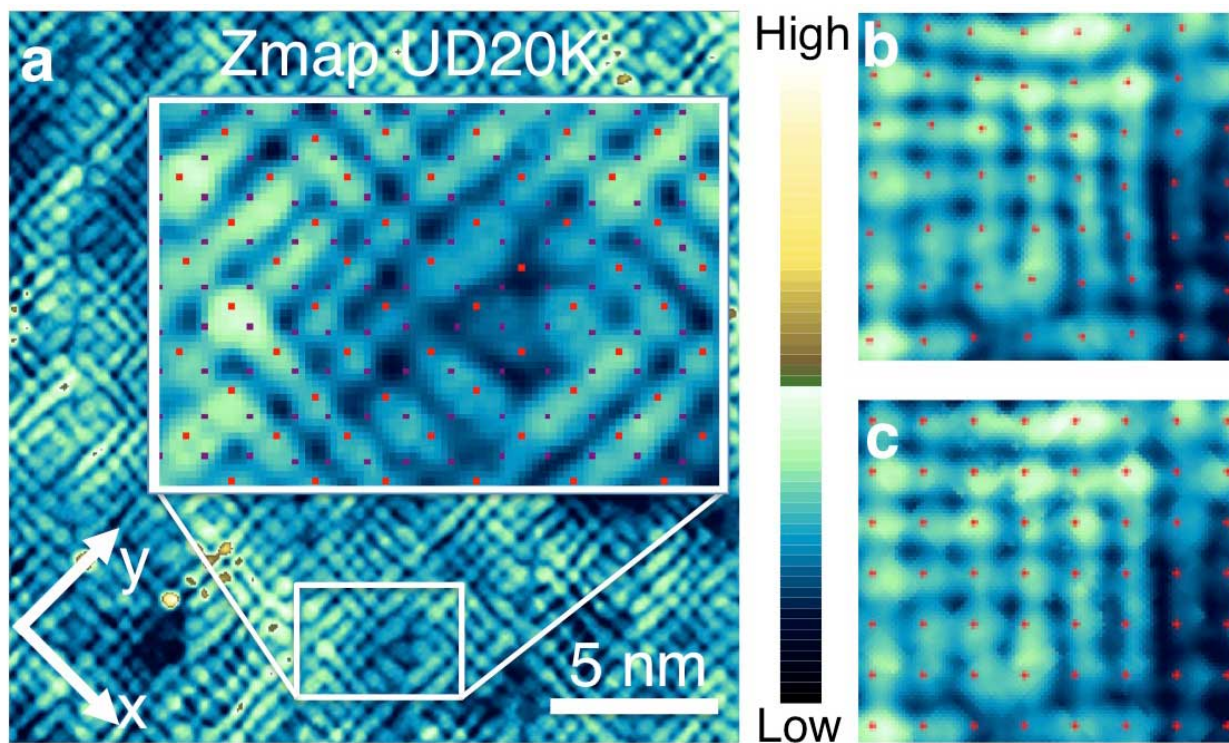
Extended Data Fig. 1 Schematic image of density waves arising from strong coupling position-based theories in CuO_2 plane. **a**, The d-symmetry $4a_0$ charge density wave. The charge density at O_x site is modulating with four-unit-cell periodicity along horizontal direction, and similarly for that at O_y but out of phase by π (d -symmetry). Cu locations are marked by small dots. **b**, The $8a_0$ pair density wave state. The d -wave Cooper pair density is modulated with eight-unit-cell periodicity along horizontal direction. Such modulation in Cooper pair density can cause $4a_0$ -period modulation in the local density of states $N(r)$.



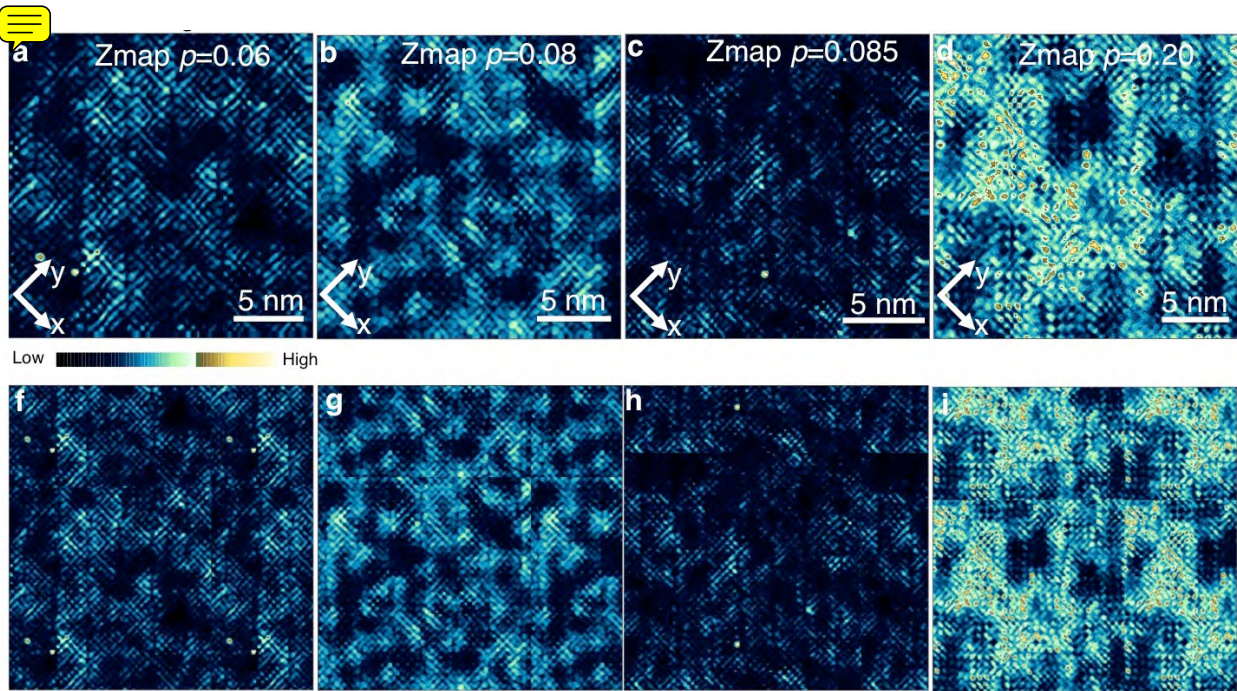
Extended Data Fig. 2 Categories defined by electronic orders. Example images from the simulated training set, from each category C , defined by d-wave form factor unidirectional modulation with wavevectors $Q_C=0.23, 0.25, 0.27, 0.29$, in units $2\pi/a_0$ (the CuO_2 unit-cell size $a_0=6$ pixels, diagonally).



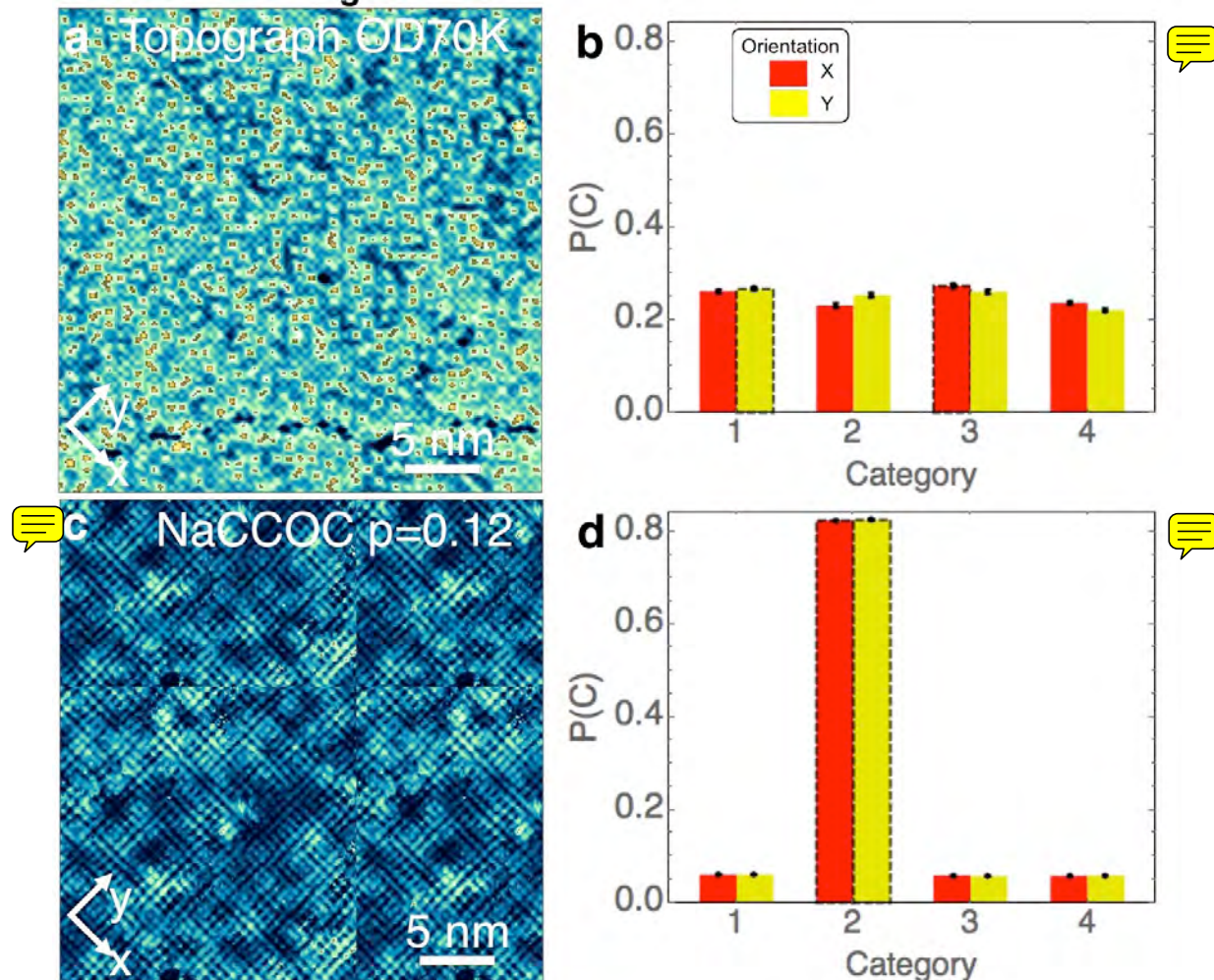
Extended Data Fig. 3 Artificial Neural Network(ANN) training and testing. **a**, Examples of the accuracy of the ANN outputs for the independent validation data set and the cross-entropy cost function is compared over different neuron activation functions during the initial training processes. The inset illustrates the non-linear activation functions - the sigmoid function and the rectified linear unit. **b**, Examples of the accuracy and the cross-entropy cost versus the number of neurons in the single hidden layer after 25 epochs of training.



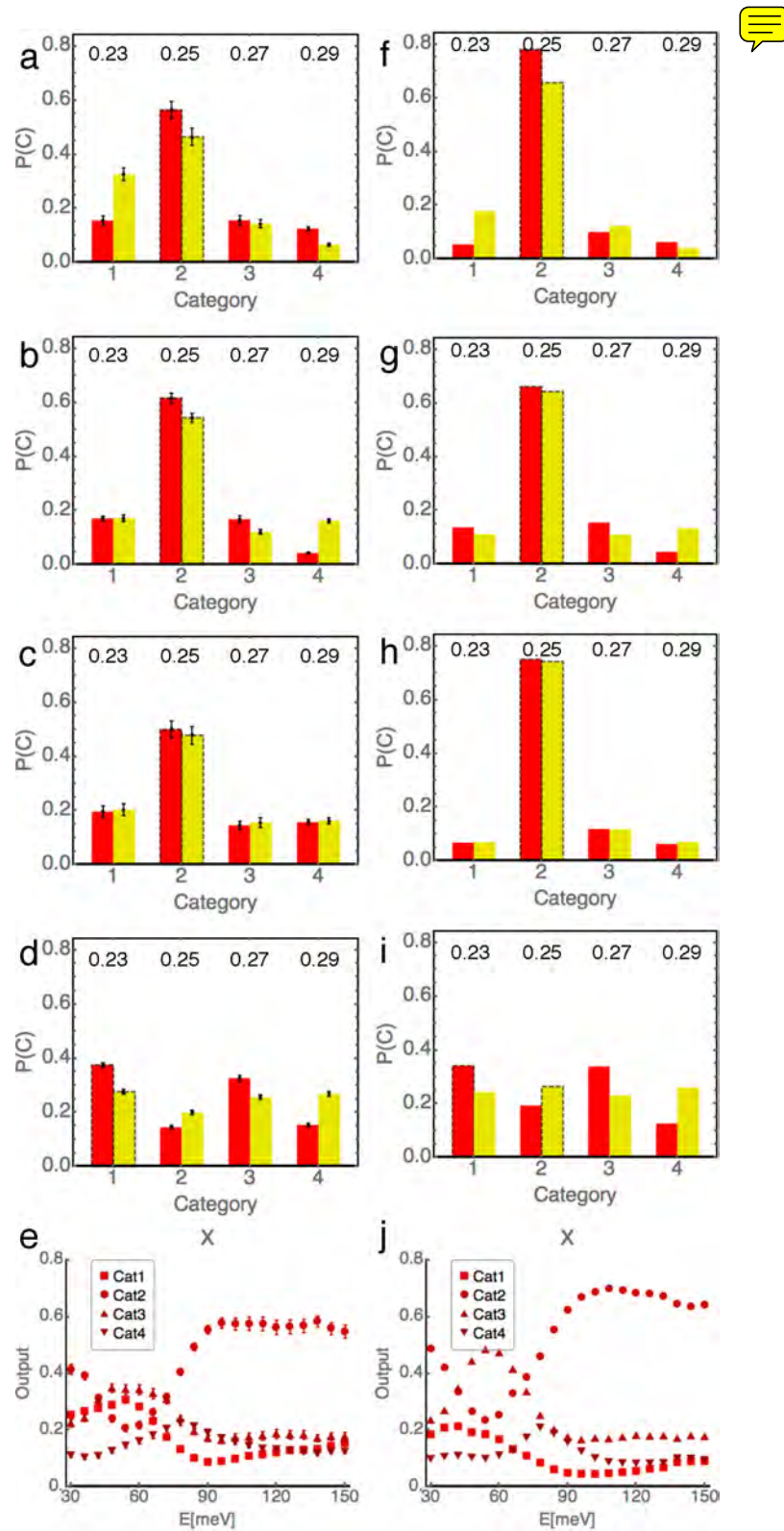
Extended Data Fig. 4 Preprocessing experimental SI-STM images. **a**, Example $Z(\mathbf{r}, E)$ of underdoped $\text{Bi}_2\text{Sr}_2\text{Ca}\text{Cu}_2\text{O}_8$ with electron density $p=0.06$ ($T_c(\text{K})=20$). The inset is a zoom-in with marked atom positions determined from topograph (Cu: red/light, O: purple/dark). **b**, A small region of **a**. **c**, The preprocessed version of **b** (see Methods).



Extended Data Fig. 5 Preprocessed experimental SI-STM images as input for categorization. **a**, The $Z(r, E)$ of underdoped $\text{Bi}_2\text{Sr}_2\text{Ca}\text{Cu}_2\text{O}_8$ with $p=0.06$ ($T_c(\text{K})=20$) at energy $E=\Delta_1$ (see main text). **f**, The preprocessed 516x516 pixel (2x86x86 CuO_2 unit-cells) input image version of **a** (see Methods). **(b,g), (c,h), and (d,i)**, The same as the pair **(a,f)** but for, respectively, underdoped $\text{Bi}_2\text{Sr}_2\text{Ca}\text{Cu}_2\text{O}_8$ with $p=0.08$ ($T_c(\text{K})=45$), underdoped $\text{Bi}_2\text{Sr}_2\text{Ca}\text{Cu}_2\text{O}_8$ with $p=0.085$ ($T_c(\text{K})=50$), and overdoped $\text{Bi}_2\text{Sr}_2\text{Ca}\text{Cu}_2\text{O}_8$ with $p=0.20$ ($T_c(\text{K})=82$). Too small images are tiled, with unit-cells intact at the tiling boundary.



Extended Data Fig. 6 Benchmarking categorization using experimental images. **a**, Topograph of overdoped $\text{Bi}_2\text{Sr}_2\text{Ca}\text{Cu}_2\text{O}_8$ with $p=0.22$ ($T_c(\text{K})=70$), preprocessed. **b**, Output categorization by 82 ANNs of **a**, showing absence of translation-breaking signal. Results for two modulation orientations X,Y are obtained by inputting to ANNs the image in **a** and its 90-degree rotated version, respectively (see Methods). **c**, The preprocessed $Z(\mathbf{r}, E)$ of NCCOC at doping $p=0.12$ at $E=150\text{meV}$, preprocessed. **d**, Output categorization by 82 ANNs of **a**, showing commensurate modulations (category 2).

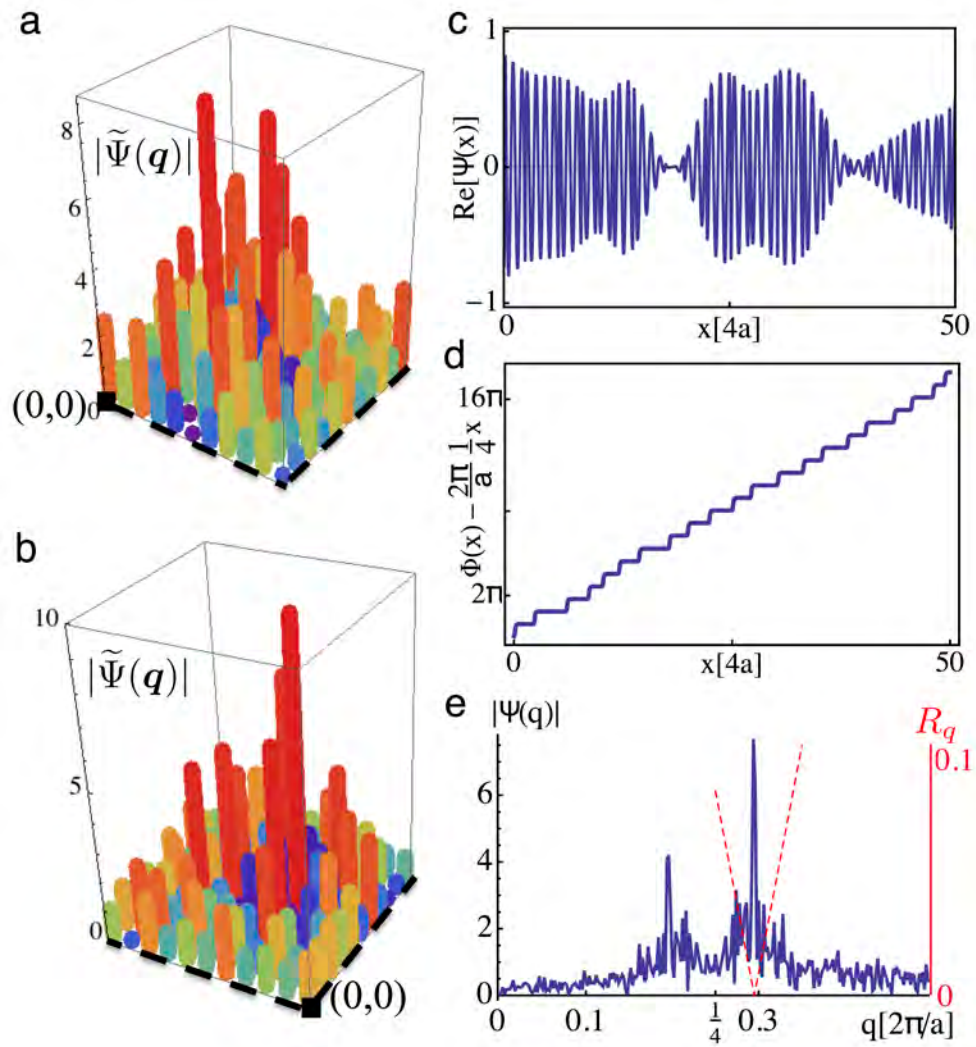


Extended Data Fig. 7 Categorization is robust to changes in training set parameters.

a-d, Output categorizations of main Figure 4I,J,K,L showing evolution with electron doping.

e, Output categorizations of main Figure 6A showing evolution with electron energy. **f-j**,

Categorizations of the same inputs as for **a-e**, respectively, but obtained from output of a single ANN trained using a different training set (see Methods).



Extended Data Fig. 8 Weakness of Fourier Transform analysis of EQM. a,b, The DFF

Fourier amplitude, $|\tilde{\Psi}(\mathbf{q})|$, with wavevector \mathbf{q} restricted to a square area with corner at the

Fourier space origin (black square) and center at $\mathbf{Q}_X = \frac{1}{4}\mathbf{G}_X$ (in **a**) or $\mathbf{Q}_Y = \frac{1}{4}\mathbf{G}_Y$ (in **b**), where \mathbf{G}_X and \mathbf{G}_Y are the Bragg peaks. Data from $\text{Bi}_2\text{Sr}_2\text{CaCu}_2\text{O}_8$ sample at doping level $p = 0.10$, ($T_c(K) = 65\text{K}$) . **c**, Modulation is the real part of complex wave $\psi(x) = A(x)e^{i(Q_0 x + \varphi(x))}$ having commensurate domains with local wavevector $Q_0 = \frac{1}{4} \times \frac{2\pi}{a}$ (period $4a$). The amplitude $A(x) \geq 0$ varies smoothly around value 1. Phase slips are incorporated in $\varphi(x)$ (see **d**). The average wavevector is $\bar{Q} = 0.3 \times \frac{2\pi}{a}$. **d**, The local phase $\varphi(x)$ of $\psi(x)$ in **c**, constructed as a discommensuration (DC) array in the phase argument $\Phi(x) = Q_0 x + \varphi(x)$. Phase slips of all DC's are set to $+\pi$. The distances between neighboring DC's vary randomly around average distance set by value of incommensurability $\delta = \bar{Q} - Q_0 = 0.05 \times \frac{2\pi}{a}$. **e**, Fourier amplitudes $|\tilde{\psi}(q)|$ of the modulation $\psi(x)$ in **c** (blue line) show narrow peak at $\bar{Q} = 0.3 \times \frac{2\pi}{a}$. The demodulation residue $|R_q|$ (red dashed line) has the minimum exactly at the average \bar{Q} .

References

- 1 Bacon, Francis, *The Advancement of Learning* (1605); republished Paul Dry Books (2001).
- 2 Gil, Y., Greaves, M., Handler, J., Hirsh, H. Amplifying Scientific Discovery with Machine Learning. *Science* **346**, 171 (2014).
- 3 AI is Changing How We Do Science, doi:10.1126/science.aan7049 (2017)
- 4 Fujita, K. *et al*, *Spectroscopic Imaging STM: Strongly Correlated Systems - Experimental Techniques* pp 73-109. Springer-Verlag Berlin Heidelberg (2015).
- 5 Carrasquilla, J. and Melko, R. G. Machine learning phases of matter. *Nature Physics* **13**, 431(2017).
- 6 Wang, L. Discovering phase transitions with unsupervised learning. *Phys. Rev. B* **94**, 195105 (2016).
- 7 Carleo, G. and Troyer, M. Solving the quantum many-body problem with artificial neural networks. *Science* **355**, 602 (2017).
- 8 Torlai, G. and Melko, R.G. Neural decoder for topological codes. *Phys. Rev. Lett.* **119**, 030501 (2017).
- 9 Van Nieuwenburg, E. P. L., Liu, Y.-H. and Huber, S. D. Learning phase transitions by confusion. *Nature Physics* **13**, 435-439 (2017).
- 10 Broecker, P., Carrasquilla, J., Melko, R. G. and Trebst, S. Machine learning quantum phases of matter beyond the fermion sign problem. *Scientific Reports* **7**, 8823 (2017).
- 11 Ch'ng, K., Carrasquilla, J., Melko, R. G. and Khatami, E. Machine Learning Phases of Strongly Correlated Fermions. *Phys. Rev. X* **7**, 031038 (2017).
- 12 Zhang, Y. and Kim, E.-A. Quantum loop topography for machine learning. *Phys. Rev. Lett.* **118**, 216401 (2017).
- 13 Deng, D.-L. , Li, X. and Das Sarma, S. Quantum entanglement in neural network states. *Phys. Rev. X* **7**, 021021 (2017).
- 14 Stoudenmire, E. M. and Schwab, D. J. Supervised learning with tensor networks. *Advances in Neural Information Processing Systems (NIPS)* **29**, 4799 (2016).

- 15 Schindler, F., Regnault, N. and Neupert, T. Probing many-body localization with neural networks. *Phys. Rev. B* **95**, 245134 (2017).
- 16 Torlai, G., Mazzola, G., Carrasquilla, J., Troyer, M., Melko, R. G. and Carleo, G. Neural-network quantum state tomography. *Nature Physics* **14**, 447 (2018).
- 17 Kivelson, S. A., Fradkin, E. and Emery, V. J. Electronic liquid-crystal phases of a doped Mott insulator. *Nature* **393**, 550 (1998).
- 18 Zaanen, J. Self-organized one dimensionality. *Science* **286**, 251 (1999).
- 19 NSF 10 Big Ideas (2016) http://www.nsf.gov/news/special_reports/big_ideas/
- 20 Ouyang, R. et al. SISSO: a compressed-sensing method for identifying the best low-dimensional descriptor in an immensity of offered candidates, *Phys. Rev. Materials* **2**, 083802 (2018).
- 21 Stanev, V. et al. Machine learning modeling of superconducting critical temperature, *Computational Materials* **4**, 29 (2018)
- 22 Rosenbrock, C. W., Homer, E. R., Csányi, G. and Hart, G. L. W. Discovering the building blocks of atomic systems using machine learning: application to grain boundaries. *njp Computational Materials* **3**, 29 (2017).
- 23 Rupp, M., Tkatchenko, A., Müller, K.-R. and Von Lilienfeld, O. A. Fast and accurate modeling of molecular atomization energies with machine learning. *Phys. Rev. Lett.* **108**, 058301 (2012).
- 24 Kusne A.G. et al. On-the-fly machine-learning for high-throughput experiments: search for rare-earth-free permanent magnets, *Scientific Reports* **4**, 6367 (2014)
- 25 Ashcroft, N. W. and Mermin N. D. *Solid State Physics* (Brooks Cole, Boston, 1976).
- 26 Keimer, B., Kivelson, S. A., Norman, M. R., Uchida, S. and Zaanen, J. From quantum matter to high-temperature superconductivity in copper oxides. *Nature* **518**, 179–186 (2015).
- 27 Wang, F. and Lee, D.-H. The Electron-Pairing Mechanism of Iron-Based Superconductors. *Science* **332**, 200-204 (2011).

- 28 Stormer, H. L., Tsui, D. C. and Gossard, A. C. The fractional quantum Hall effect. *Rev. Mod. Phys.* **71**, S298 (1999).
- 29 Balents, L. Spin liquids in frustrated magnets. *Nature* **464**, 199–208 (2010).
- 30 Orenstein, J. and Millis, A.J. Advances in the Physics of High-Temperature Superconductivity. *Science* **288**(5465):468–474 (2000).
- 31 Norman, M. R., Pines, D. and Kallin, C. The pseudogap: friend or foe of high T_c? *Adv. Phys.* **54**, 715-733 (2005).
- 32 Fradkin, E. *et al.* Nematic Fermi Fluids in Condensed Matter Physics. *Annual Review of Condensed Matter Physics* **1**, 153-178 (2010)
- 33 Fradkin, E., Kivelson, S. A. and Tranquada, J. M. Colloquium: Theory of intertwined orders in high temperature superconductors. *Rev. Mod. Phys.* **87**, 457 (2015).
- 34 Bianconi, A *et al.* Stripe structure in the CuO₂ plane of perovskite superconductors. *Phys. Rev. B* **54**, 12018 (1996).
- 35 Comin, R. and Damascelli, A. Resonant X-Ray Scattering Studies of Charge Order in Cuprates. *Ann. Rev. of Condensed Matter Physics* **7**:369-405 (2016).
- 36 Fujita, K. *et al.* Direct phase-sensitive identification of a d-form factor density wave in underdoped cuprates. *Proc. Nat'l. Acad. Sci.* **111**, E3026–E3032 (2014).
- 37 Forgan, E. M. *et al.* The microscopic structure of charge density waves in underdoped YBa₂Cu₃O_{6.54} revealed by X-ray diffraction. *Nature Communications* **6**, 10064 (2015).
- 38 Comin, R. *et al.* Symmetry of charge order in cuprates. *Nature Materials* **14**, 796–800 (2015).
- 39 Hamidian, M. H. *et al.* Atomic-scale electronic structure of the cuprate d-symmetry form factor density wave state. *Nature Physics* **12**, 150 (2016).
- 40 Mesaros, A. *et al.* Commensurate 4a0-period charge density modulations throughout the Bi₂Sr₂CaCu₂O_{8+x} pseudogap regime. *Proc. Nat'l. Acad. Sci.* **113**, 12661-12666 (2016).
- 41 Robertson, J. A. *et al.* Distinguishing patterns of charge order: Stripes or checkerboards. *Phys. Rev. B* **74**, 134507 (2006).

- 42 Del Maestro, A., Rosenow, B. and Sachdev, S. From stripe to checkerboard ordering of charge-density waves on the square lattice in the presence of quenched disorder. *Phys. Rev. B* **74**, 024520 (2006).
- 43 Nielsen, M. A. *Neural Networks and Deep Learning* (Determination Press, 2015); <http://neuralnetworksanddeeplearning.com>.
- 44 Rumelhart, D. E., Hinton, G. E. and Williams, R. J. Learning representations by back-propagating errors. *Nature* **323**, 533-536 (1986).
- 45 Cover, T. M., and Thomas, J. A. *Elements of Information Theory* (2nd Edition, Wiley, 1991).
- 46 Nie, L. et al. Quenched disorder and vestigial nematicity in the pseudogap regime of the cuprates PNAS **111** 7980-7985 (2014)
- 47 Chaikin, P.M. and Lubensky, T.C. *Principles of Condensed Matter Physics*, Cambridge University Press (1995).
- 48 Cybenko, G. Approximation by superposition of a sigmoidal function. *Math. Control Signals Systems* **2**, 303–314 (1989).